UHASSELT
KNOWLEDGE IN ACTION

Maastricht University

Faculty of Medicine and Life Sciences
School for Life Sciences
Master of Biomedical Sciences

Masterthesis

Luminescent nanodiamonds: solution for precise molecular detection

Louis Kruyfhooft

Thesis presented in fulfillment of the requirements for the degree of Master of Biomedical Sciences, specialization Bioelectronics and Nanotechnology

SUPERVISOR :
Prof. dr. Milos NESLADEK

CO-SUPERVISOR :
de heer Michal GULKA

2017
2018

Transnational University Limburg is a unique collaboration of two universities in two countries: the University of Hasselt and Maastricht University.

UHASSELT
KNOWLEDGE IN ACTION

www.uhasselt.be
Universiteit Hasselt
Campus Hasselt:
Martelarenlaan 42 | 3500 Hasselt
Campus Diepenbeek:
Agoralaan Gebouw D | 3590 Diepenbeek

UHASSELT
KNOWLEDGE IN ACTION

Maastricht University

Faculty of Medicine and Life Sciences
School for Life Sciences
Master of Biomedical Sciences

Masterthesis

Luminescent nanodiamonds: solution for precise molecular detection

Louis Kruyfhooft

Thesis presented in fulfillment of the requirements for the degree of Master of Biomedical Sciences, specialization Bioelectronics and Nanotechnology

SUPERVISOR :
Prof. dr. Milos NESLADEK

CO-SUPERVISOR :
de heer Michal GULKA

Acknowledgements

First, I would like to spend some words directed towards the people who helped me during my thesis. I would like to express my great appreciation to my mentor Michal Gulka. With a bachelor's degree in biology, it wasn't self-evident to start a master thesis in quantum physics. However, from the beginning, he helped me with everything I didn't understand. Starting from literature study to the experiments I had to master, he always stood by my side when problems arose. Moreover, I want to thank him for all the time he spent on correcting and advising me with presentations, interim reports and of course the final thesis. He gave up his spare time when necessary, which I deeply appreciate.

Big thanks also go to my promotor Professor dr. Miloš Nesládek who gave me the opportunity to start working on a very unique and promising subject. Despite his tight time schedule, he also gave up a lot of time on correcting and advising me concerning my master thesis, presentations and interim reports.

Of course, I want to thank my parents, friends, colleagues and all the persons in my research group who helped me during these 8 months. Especially to Simon Denis, who was always ready to bring me to IMO by car from the moment I broke my heel bone. Also to dr. Emilie Bourgeois and Jaroslav Hrubý I want to express my thanks since they were always there helping me on the set-up when Michal wasn't available.

At last I also want to thank IMO for their trust and giving me the opportunity to work in their laboratories.

Abbreviations

AOM:	Acousto-optic modulator
APD:	Single-photon avalanche photo-diode
CVD:	Chemical vapor deposition
CW:	Continuous Wave
EPR:	Electron paramagnetic resonance
HPHT:	High-pressure high-temperature
ISC:	Intersystem crossing
MW:	Microwave
ND:	Nanodiamond
NV:	Nitrogen vacancy
ODMR:	Optical detected magnetic resonance
PCB:	Printed circuit board
PSB:	Phonon side band
ROS:	Reactive oxygen species
T_1:	Spin-lattice relaxation time
ZFS:	Axial zero-field splitting
ZPL:	Zero phonon line

Abstract

Quantum sensing is anticipated to bring a ground-breaking understanding of life cycle processes thanks to high sensitivity, specificity and resolution. One of the possible quantum sensing platforms are nanodiamond particles (NDs) containing nitrogen-vacancy (NV) centres – defects in the diamond lattice that are extremely sensitive to surrounding magnetic fields. Here we aim to establish a quantum sensing detection method based on NV spin relaxation time (T_1) readout from NDs using optically detected magnetic resonance (ODMR). This will enable future detection of reactive oxygen species (ROS) using NDs covered with superoxide-specific spin-traps, where the sensing principle is based on the variation of the T_1 upon ROS attachment. For the establishment of pulsed-ODMR measurements, single-crystal diamond and NDs of 5-60 nm in size containing NV centres are used. The measurements are performed with a home-built confocal microscope modified to enable pulsed experiments. NV spin transitions are induced with microwaves (MW) applied to the sample either by wire or by MW antenna. The MW pi-pulse is determined from Rabi measurements. For the relaxometry we use a laser pulse (NV initialization and readout) followed by a microwave pi-pulse (NV spin excitation). The T_1 values are obtained from data fitting. I have successfully measured ODMR from NDs both, dried on a cover slip and directly in colloid. For the liquid measurement I have built a specific sample holder to allow microwave excitation directly in water while using a high N.A. objective. The ODMR parameters have been optimized in terms of laser and microwave power. Furthermore, I have developed pulsed protocols for Rabi and T_1 measurements and calibrated them on single-crystal diamond and later applied them to nanodiamond particles. Finally, the NDs has been modified with nickel sulfate to observe a change in T1 and to confirm the sensing principle.

Introduction

A complete understanding of cellular processes, which take place in disease development, would be incredibly beneficial for human health and lifespan. Unfortunately, this remains still an utopia as the classical detectors lack the requisite sensitivity or/and resolution. Cancer for example, cause each year the dead of millions of people (1). Despite this large number, a lot is still to be learned about this disease. A link between overproduction of superoxide radicals (O_2^-) to cancer has been already suggested (2). Still it is very hard to predict which exact interactions between the superoxide radicals and cell compartments take place. The metabolism of oxygen results in reactive oxygen species (ROS), which include superoxide radicals (3). These ROS play an important role not only in homeostasis, but also in cell signaling and cell aging (4). Overproduction of ROS due to cell stress can lead to cell damage and consequently give rise to multiple diseases (5). Quantitative and spatially-resolved detection of superoxide radicals (and ROS in general) would provide insights in the disease development. However, this remains challenging due to their high reactivity and ephemeral behavior. If the detection of ROS becomes possible, the pathway and different interaction sites in the cell can be resolved. This would provide us with new insights for cell aging, cancer and other related diseases.

Several methods for ROS detection are currently available, however each with their own drawbacks with the main problem of low sensitivity, the specificity and the lifetime of such probes. A first example are chemiluminescent probes. These probes bind onto ROS and will emit light when the reaction occurs. These probes are easy in use; however, they are non-specific and will have the affinity for several ROS molecules (6). Another possibility are fluorescent probes which are also used for a large variety of different molecules including ROS. Unlike chemiluminescence, where an electron is in a high energy state due to the chemical reaction leading to creation of an unstable intermediate, the electron in fluorescence is excited due to the absorption of a photon. By binding on the target molecule, fluorescence can be used indirectly as a probe for tracing ROS molecules. Problems arise when multiple chemical products can be formed between probe and target molecule. This results in an overlap of the fluorescent spectra of the different products. Distinction between these different probe-target complexes is almost impossible. The standard confocal techniques have a resolution of around 300 nm and can be used for in situ ROS production measurements (7). However, the dyes tend to lose their stability over time and bleach.
Looking at the fundamental question in this thesis: can we use ROS electron spin for the ROS monitoring and use chemical traps to bind the ROS on the nanoprobe surface? The related question is whether such spin trapping give us a better alternative? To address this question, we developed a general method for the detection of electron spins carrying a molecule, using the T1 spin relaxometry.

A spin trap is a chemical compound which we define as a substance that has an ability to stabilize or trap free radicals by forming a covalent bond with the target molecule resulting in a spin trap-molecule complex. Due to slow rate constants, higher concentrations of the spin traps at the probe surface can be achieved then free ROS that come into the interaction with the probe. Currently there is no such ROS detection technique available that would allow for spatially-resolved and real-time measurements of ROS in intra-cellular environment.

In this thesis, a novel general method for measurement of concentration of electron spin carrying species is proposed. The idea is to use a nanodiamond (ND) sensor instead of fluorescent and chemiluminescent probes. The ND sensing capabilities lay within the impurities incorporated in the lattice structure. Such impurity is a lattice defect called Nitrogen Vacancy centre. These nitrogen vacancy (NV) centers give the NDs unique optical properties, which are used for the spin detection. Owing to their nano-metric size, biocompatibility and optical properties, the NDs are vastly studied for applications such as drug delivery (8) , thermometry (9) , bio-imaging (10) and very recently quantum sensing in cells (11). Here a quantum sensor based on NDs covered with spin traps, to achieve high specificity, is proposed. Attachment of the target molecule onto the with spin trap covered NDs will result in paramagnetic complexes. Due to interaction of such paramagnetic species with the NV spins, this results in a change of NV spin relaxation time that can be monitored (12). Because the NV centre is read by using spin coherence methods we call them quantum sensors. The use of quantum sensor would allow for precise location of the target molecule with confocal resolution and high sensitivity and specificity, making this quantum sensor a very promising tool for example superoxide molecule detection directly in live cells. Specifically, only those ROS that bind selectively to the ND probe are detected. While the sensor development requires a large team work, the first goals dealt with here is to develop the spin detection technique on its own.

Aims of the thesis

The main aim of this work is enabling a quantum sensing detection method based on NV spin relaxation time (T_1) readout from nanodiamond particles using pulsed optically detected magnetic resonance (ODMR). This includes modification to the existing optical confocal setup and development and optimization of the pulsed sensing protocols. The main output of the thesis is establishment of routine T_1 readout from NDs as a first step towards development of envisaged cellular quantum sensors.

Following goals will be established:

- Development of a sample holder which allows for ODMR measurements in liquid.
- Detection of CW-ODMR signal from NDs in liquid.
- Setup modification and pulsed sequence development to enable pulsed-ODMR
- Establishment of Rabi and T_1 measurements on single crystal diamond
- Pulsed sequence optimization for quantum measurements on NDs.
- Establishment of routine T_1 readout from NDs and demonstration of the quantum sensing possibilities of NDs.

Nanodiamond

Properties

Nanodiamonds are well known for their unique and diverse properties. The lattice structure of a nanodiamond consists of a dense carbon sp^3 configuration, resulting in a very durable and chemically inert material. Optical properties are unique due to a relatively high index of refraction of diamond and thanks to the implementation of impurities into the diamond lattice such as nitrogen and other color centers, which yield over time stable luminescent signal. Together with biocompatibility (13), non-toxic behavior (14) and the ability to tune their surface structures (15) NDs are employed for numerous different applications. Some of the examples include drug delivery, bioimaging (16), tissue engineering (17) or recently quantum sensing (12). Thanks to their size that can vary from a few to hundreds of nm, NDs can be easily internalized in cells via clathrin-mediated endocytosis (18). Furthermore, the production-cost of these little diamonds is relatively cheap (19) and NDs are commercially available.

Synthesis

ND's can be produced using different synthesizing methods. Detonation, chemical vapor deposition (CVD) and the high-pressure high-temperature synthesis are the three main production methods used nowadays.

Detonation

During the detonation synthesis method, explosive energy is used for ND production. In most cases, the carbon source is delivered by the explosive itself, otherwise, a carbon source is brought in a metal chamber together with the explosive. As an explosive, a mixture of 40% trinitrotoluene (TNT) and 60% hexogen (RDX) is commonly used (20). A gas e.g. N_2 or liquid e.g. water is used as a cooling medium. Due to the explosion, ideal conditions such as high temperature and high pressure are created for the formation of diamond. To obtain pure nanodiamonds particles, sufficient de-aggregation and purification steps are required (21).

CVD

CVD synthesis is usually used to obtain ultrapure nanodiamonds. Due to the fact that diamond is grown in thermodynamically instable region of the carbon phase diagram, the CVD growth of diamonds is also referred to as a metastable synthesis method. Due to the kinetic factors, growth in these thermodynamically instable region of the phase diagram, is still possible (22). Methane (CH_4) and hydrogen (H_2) are brought together in a stainless-steel deposition chamber. Heating at temperatures above 800 °C and application of MW plasma results in the decomposition of methane resulting in the formation of a diamond layer. Addition of other molecules, such as nitrogen, will result in the incorporation of impurities in the lattice structure of the diamond. ND particles are created by milling the diamond layers (23).

HPHT

During the high pressure – high temperature (HPHT) synthesis method, a carbon source material is subjected to temperatures above 1500 °C and a high pressure above 5 GPa. Under these circumstances, the graphite will be transformed into diamond due to realignment of the carbon bonds. A catalyst, usually metal solvents, can be used to lower the required formation energy. However, a catalyst will result in less pure nanodiamonds (24).

ND's are still to be modified to create the NV centers. Single nitrogen defects are already incorporated in the lattice structure of HPHT diamond, however irradiation with a high-energy ion beam is necessary to create the vacancies. After the irradiation, NDs are annealed at high temperatures (above 600 °C), in which vacancies become mobile and can be trapped by nitrogen to form thermally stable NV centres. A last step is the oxidation of nanodiamond surface that leads to a stabilization of the NV^- centers (25) and helps to prevent aggregation in colloid. A complete prevention of agglomeration can be achieved by using silica shells (26).

Nitrogen vacancy (NV) center

The NV center complex (see figure 1) consists of a nitrogen atom which is bonded covalently to three neighboring carbon atoms.

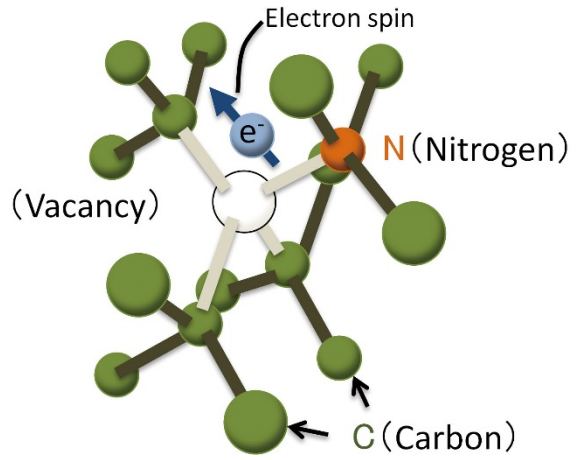

Figure 1: A nitrogen-vacancy (NV) center in diamond. Taken from (27).

Since nitrogen has five valence electrons, a lone electron pair is still present. The vacancy itself holds three free electrons from the surrounding carbon atoms. Two of these free electrons make a pair with the lone pair present at the nitrogen atom. One electron now remains at the vacancy (28), however, in the NV^- state an additional donor electron is present. This extra electron is believed to come from a neighboring nitrogen impurity (29).

Multiple charge states of NV centers are known to be present in diamond. The two most common charge states are the neutral NV center presented with NV^0 and the negatively charged NV center NV^-. A third type of NV center is the one which is positively charged; NV^+, however this last one isn't completely understand yet and is irrelevant in this thesis as it does not exhibit any photoluminescence. Due to the special characteristics of a negatively charged NV center, such as the possibility of an optical read out of its electronic spin state and the optical spin initialization to a known state, NV^- is exploit for quantum sensing applications (30).

NV^- electronic structure

The NV^- center consists of a spin triplet with C3v symmetry, which corresponds to the 6 electrons in the system. In a spin triplet state, two electrons with parallel spins are present in different molecular orbitals (31). Multiple electronic configurations of the electronic spin states are possible and are represented by $^1A_1$, $^3A_2$, ^1E and ^3E (32). The type of symmetry of the system is represented by A_1, A_2 and E, while the allowable number of m_s spin-states are depicted by the upper digits (1 and 3). It has been found that the ground state of a NV^- center consists of a spin-triplet with a $^3A_2$ symmetry (33). This spin triplet can be split into two lower states $a_1(1)$ and $a_1(2)$, which are fully occupied, and two degenerate orbitals e_x and e_y which are populated by one unpaired electron (34). Due to axial zero-field splitting (ZFS) of the spin triplets, resulting from the spin-spin interaction between the unpaired electrons, the $m_s=0$ and $m_s=\pm1$ states are separated by 2,87 GHz (35). The promotion of an electron from the $a_1(2)$ orbital to the $e_{x,y}$ orbital results in an excited state, which is represented by the spin-triplet ^3E state. Here the resulting ZFS is 1,42 GHz.

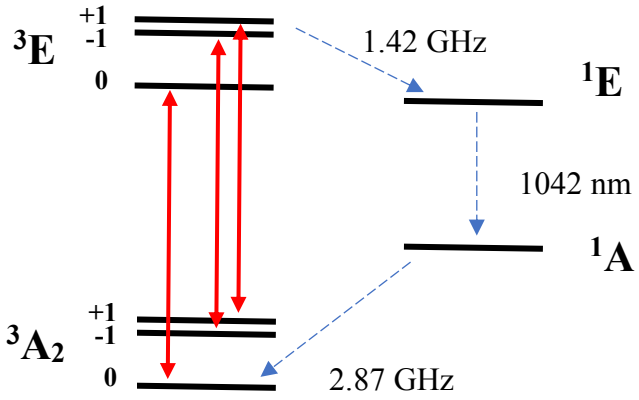

Figure 2: Energy level diagram for the NV^- center. The spin-triplet ground ($^3A^2$) and excited (^3E) states are depicted on the left, the singlet system involved in ISC is depicted right. The solid red arrows represent radiative transitions while the dotted arrows represent the non-radiative decay.

The excitation of electrons from the $^3A_2$ ground state to the ^3E excited state can be realized by applying a green laser beam (532nm) on the NV center. For most efficient excitation, the application of the laser beam must be in parallel to the NV axis (36). From the excited state, the electron can decay either by emitting a red photon or non-radiatively via metastable single state (^1E and $^1A_1$ with spacing of 1042 nm (37)) by intersystem crossing (ISC). The decay via ISC is also called "dark

transition" as no red photon is emitted (see figure 3). Transitions of the electrons in between ground and excited states are spin conserving with exception of the non-radiative decay trough the metastable singlet state. This decay is preferential for the electrons with $m_s=\pm1$ spin and here the transition of the spin population from the $m_s=\pm1$ to $m_s=0$ occurs. This ISC can be explained by spin-orbit coupling which results from the interaction between the magnetic field and the spin magnetic moments of the electrons.

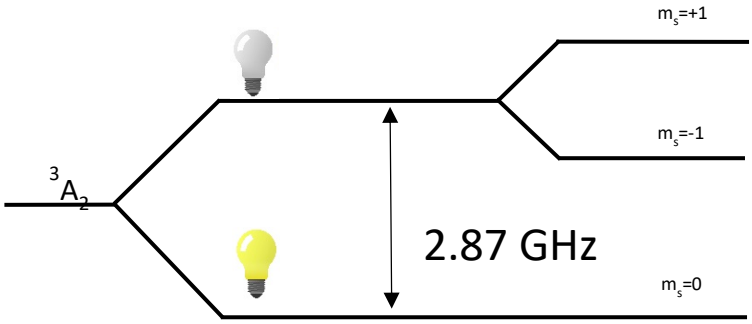

Figure3: schematic representation of electronic sublevels where $m_s=0$ is the so-called bright state and $m_s=\pm1$ the dark state.

After excitation of an electron out of the $m_s=0$ ground state, the electron decays straight back to its initial state ($m_s=0$ ground state). On the other hand, when the electron is in the $m_s=\pm1$ excited state, a decay to the $m_s=0$ sublevel of the $^3A_2$ ground state ("dark transition") will occur in 30% of the cases and thus the luminescence signal is lowered. Due to these characteristics NV^- centre holds two important features: 1) It can be optically pumped to the $m_s=0$ ground state after a few cycles of excitation, which is called spin polarization (see figure 4); 2) Optical read-out of the spin state based on the difference in luminescent intensity is possible.

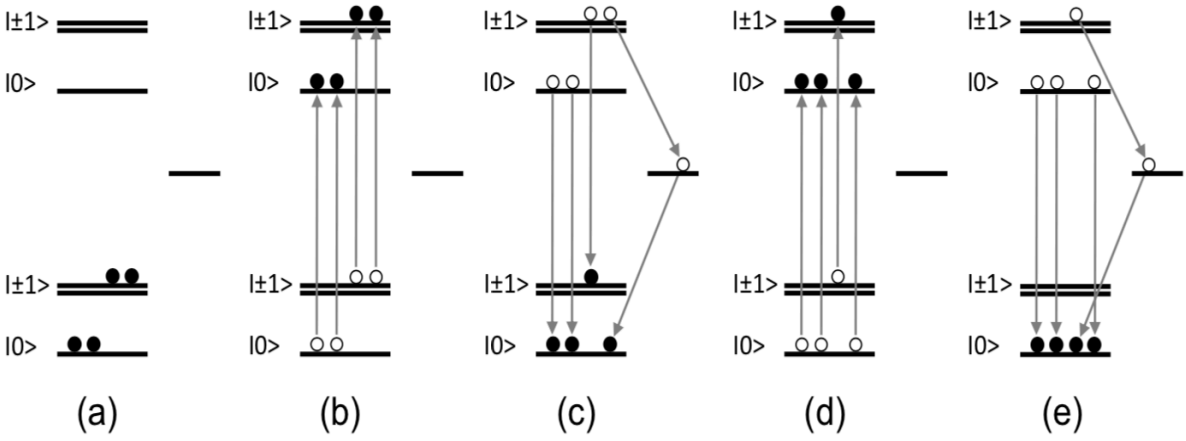

Figure 4: Schematic representation of the optical pumping mechanism of a NV^- center. a) At room temperature the $m_s=0$ and $m_s=\pm1$ spin states are equally populated. b) Spin conserving green laser excitation to the excited state. c) Due to ISC, 30% of the $m_s=\pm1$system will fall back non-radiatively to the groundstate via the intermediate singlet energy level. d) Another excitation cycle. e) The system is fully polarized into the $m_s=0$ state after enough excitation cycles are applied.

The occupation of the different sublevels can be manipulated by applying resonant microwaves onto the sample. When these microwaves are at resonant frequency the population of the electrons in the $m_s=0$ and $m_s= \pm 1$ state are flipped (38). The difference in fluorescent signal can be visualized using optically detected magnetic resonance (ODMR) as will be explained later in this thesis. When an external magnetic field is applied, Zeeman Effect will lead to an energy splitting between the $m_s=\pm 1$ sublevels (39). The larger the applied magnetic field is, the larger the splitting will be. Looking at the NV centers, four different orientations exist, each along the crystallographic axes. Dependent on the angle between the magnetic field and the NV axis, a different splitting will occur. Since in single crystal diamonds, the magnetic field can be applied along the four different orientations of the NV-centers, a maximum splitting of eight peaks can be obtained. The situation is however bit different for ND particles. Due to the random mutual position of the NDs, the orientations of the NV centers are random amongst the nanodiamond sample. This often results in unobservable sharp resonant lines when magnetic field is applied to NDs and the signal is collected from ensemble of many particles.

Photoluminescence

Organic dyes and fluorophores are commonly used for imaging purposes. However, due to photobleaching they can't be used for long-term measurements. Additional quantitative measurements are difficult. Nanodiamonds, however, have shown to overcome these problems. Due to the embedded NV centers, ND's have uniquely stable photoluminescent properties. These ND's show no photo-bleaching problems, there is no blinking behavior and they are perfectly photostable. Another advantage is that ND's can easily penetrate into cells. This in combination with a good biocompatibility makes the ND's ideal for in vivo imaging (40). The NV fluorescence spectrum ranging from 550 nm to 800 nm (see figure 5) of NV centers is quite broad (41) mainly due to large red-shifted phonon side bands (PSB) and also due to the overlap of both, and NV^-. The zero-phonon line (ZPL) of the NV^0 and NV^- center is 575 nm and 637 nm respectively, which corresponds to their electronic transition between the excited state and the ground state.

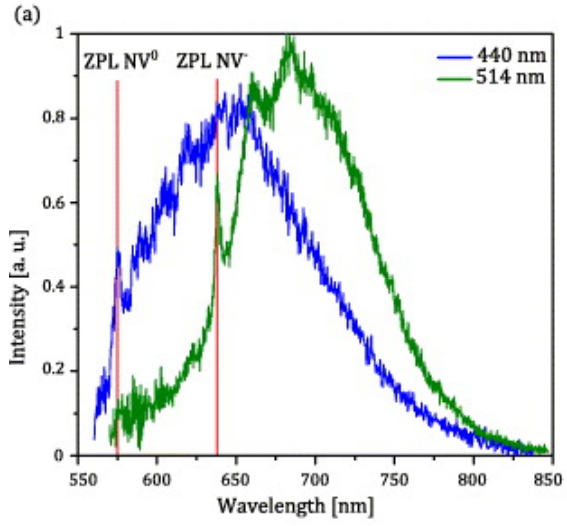

Figure 5: Photoluminescence spectrum of NV^0 and NV^-. ZPL's are visible at 575 nm (NV^0) and at 637nm (NV^-). Taken from (48)

Optical detected magnetic resonance (ODMR)

In ODMR experiments, optical detection is used for the determination of the magnetic resonances. The ODMR is in principle similar to electron paramagnetic resonance (EPR), but the detection principle is purely optical. In both the signal is obtained by applying a constant magnetic field and varying the microwave frequency on the sample or vice versa. In EPR microwave absorption is detected as the signal, whereas in ODMR the resonances are observed by different photon count. For the detection of small differences in the electronic spin state, EPR needs high magnetic fields and high MW frequencies (42). In this respect, ODMR spectra are much easier to obtain experimentally for NV centers.

Continuous-wave (CW) ODMR

Using ODMR, the multiple electronic spin states can be optically visualized. ODMR measurements are performed by sweeping the microwave frequency and in the same time collecting the luminescence signal. When the microwave is at resonance frequency, a drop in fluorescence is present due to the fact that the electrons are driven into the dark state ($m_s=\pm1$). Applying an external magnetic field will lead to two (or more depending on the B-field orientation) different resonant frequencies, which represent the transitions of $m_s=0$ to $m_s=-1$ and $m_s=0$ to $m_s=+1$ respectively. The larger the applied magnetic field, the larger the splitting will be (43). Using pulsed measurements, background noise can be eliminated, which leads to higher contrast compared to CW measurements (42).

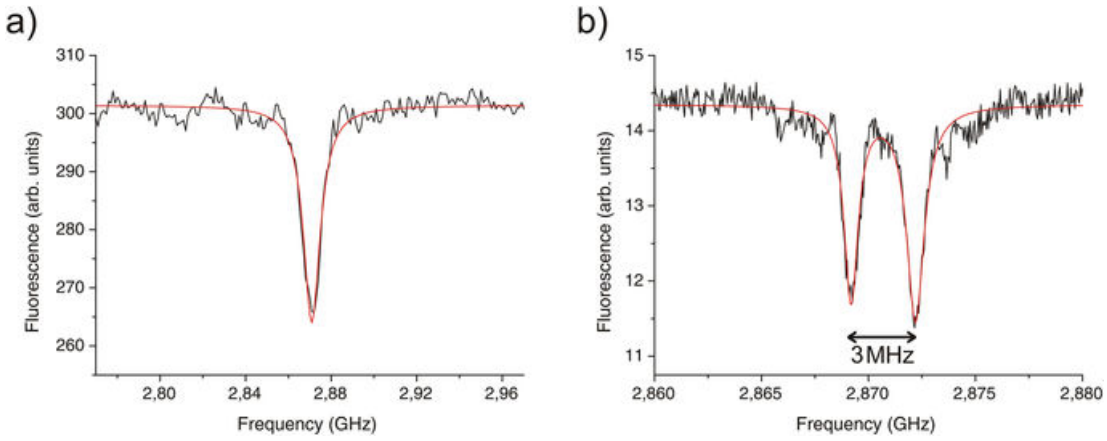

Figure 6: Measured ODMR spectra without external magnetic field (a) and with an external magnetic field applied perpendicularly onto the 100 diamond lattice orientation (b).

Pulsed-ODMR

In comparison to CW-ODMR, pulsed-ODMR is necessary for obtaining some sensing schemes such as Ramsey fringes, Hahn-echo, Rabi nutations and T_1 relaxometry measurements. In pulsed-ODMR, spin initialization and spin readout are separated in time which reduces the power broadening effect (29). The reduction in power broadening effect leads to increased sensitivity of pulsed-ODMR measurements compared to CW-ODMR. Multiple quantum sensing protocols including detection of nuclear spins by NMR and MRI are pulsed. Therefore, it is necessary to use different quantum sensing sequences. Ramsey fringes for example, are used for the determination of the dephasing time T_2^* and is implemented for DC magnetometry (44). Enhancement of the sensitivity can be obtained via Hahn-echo measurements by measuring the decoherence time T_2, whereby a π-pulse is implemented within Ramsey fringes measurements, making this sequence sensitive to AC magnetic fields (45). Other examples are Rabi nutations and T_1 relaxation time measurements which were performed in this thesis using pulsed-ODMR and are described in detail in following subchapters.

Rabi nutations

A Rabi sequence is a quantum pulsed protocol used to characterize the qubit and to obtain the duration of the MW π-pulse. The measurements consist of a laser pulse used for NV polarization to the m_s=0 spin state, followed by a resonant MW pulse for NV spin manipulation and lastly an additional laser pulse for the readout of the NV spin state (see Figure 7a). The resonant MW pulses in Rabi-oscillation measurements induce the flipping between the m_s=0 and m_s=±1 spin states. Varying the length (τ) of the MW pulse at a fixed laser and MW power and collecting the photon signal for each τ will induce the oscillations of the obtained signal (29). For each MW length, multiple (thousands) measurements are performed and averaged out. The resulting Rabi nutations are depicted in Figure 7b. First all NV spins will be in the bright state, resulting in a high luminescence signal. By increasing the MW length, more NV spins will be flipped into the dark state. When the MW pulse is long enough the luminescence will be in a minimum, whereby all the NV spins are positioned into the dark state. This pulse duration that flips the spin orientation for specific MW power is called the π-pulse. A further increase in length of the MW, will cause the luminescence to increase again because the NV spins will be driven again into the bright state by stimulated emission and so on.

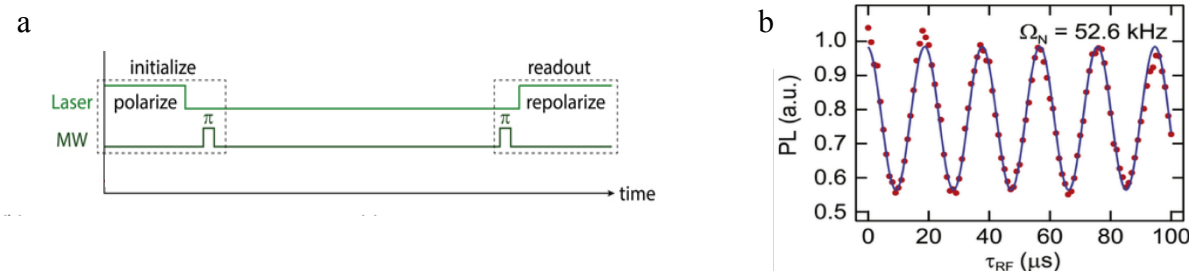

Figure 7: a) Example of a pulse scheme for Rabi nutation measurements. b) Rabi oscillations. Taken from (51)

NV^- spin relaxation time

Spin relaxation is characterized via two different time scales. The T_1 or longitudinal relaxation time and the T_2 or transverse relaxation time. In this research, only the T_1 time will be used. When nuclear or electron spins are flipped from parallel to anti-parallel along the magnetic field, they come in a higher energy state. Since the lowest energy state is preferred, they have a tendency to reduce their energy and fall back to their original energy state. This process is called spin relaxation. The time needed for these nuclear or electron spins to fall back to their ground state is called the spin relaxation time.

The T_1 time, also called the spin-lattice relaxation time, arises from the rearrangement of the magnetization vector along the z-axis and results from the release of energy to the lattice (environment) (46). Different processes such as Raman, Orbach and dipole-dipole interactions can be involved in this mechanism. During the T_1 relaxation, spin states, which were first polarized, will fall back into the thermally mixed state. The time needed for this process is called then the T1 time, which can be measured experimentally. The T_1 time is sensitive to temperature, but also to surrounding fast fluctuating magnetic fields. Looking at ND's, the T_1 is relatively long for bulk diamond (several milliseconds), which makes it easier to measure. For NDs the t1 time is typically about 10 -100 times lower.

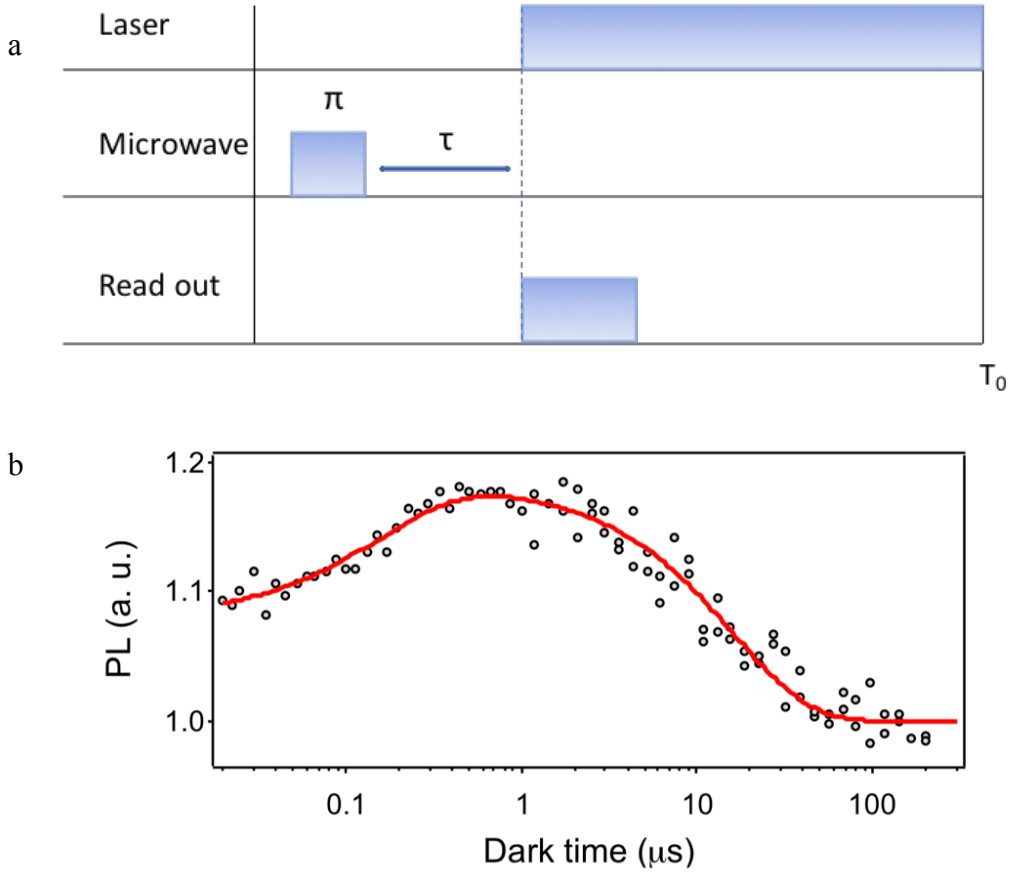

Figure 8: a) Schematic representation of a pulse scheme used for T_1 measurements. b) T_1 signal after applying the pulse scheme taken from (59).

Quantum sensing with nanodiamonds

In past few years, nanodiamonds have been shown to be very useful in quantum sensing applications. Optical detection of very weak magnetic fields via nitrogen vacancy centers in NDs for example, has opened new frontiers in biology and physics (47). Since NDs are perfectly biocompatible and have unique luminescence properties, they are also used as fluorescent probes. Due to their high stability and resistance to photobleaching, they have been shown to be more useful compared to conventional techniques (48). In this thesis, principle of ROS detection via T1 sensing on NDs is proposed and the sensing mechanism will be examined. ROS molecules are an important group of radicals which play a major role in different disease developments. A better understanding of these molecules can lead to a breakthrough in treatment and prevention. However, because of their high reactivity they are hard to detect. Surface modification of NDs with spin traps specific for these ROS molecules may lead to a new sensing device. Since spin traps have a high specificity and high affinity, ROS molecules can be trapped with a great efficiency. Via optical measurements on the ND, the T1 time can be determined. A change in T1 time upon binding could potentially allow to detect these high reactive radicals or other molecules onto the ND surface, resulting in a ND quantum sensor for single molecule detection.

Materials and methods

Nanodiamonds

For the purpose of this master thesis commercial NDs are used, produced by the high-pressure high-temperature (HPHT) method, resulting in NDs of a size-range between ~5 to 50 nm with single-substitutional nitrogen as a main impurity. To prevent stacking, resulting in agglomerate formation, the ND's are coated with a silicon layer. Nitrogen impurities are already incorporated in the lattice structure of the diamonds, but to form the NV centers, NDs are first irradiated by high-energy ion beam to create the vacancies and afterwards annealed at high temperatures (900 °C for one hour). Annealing will cause the vacancies to move through the ND's lattice structure until they are trapped by a nitrogen atom creating a stable nitrogen vacancy complex.

Home-built confocal microscope set-up

For the measurements on the diamonds, a home-built confocal microscope set-up was used. A Gem 532 laser is used as a laser-source for NV excitation. Single-photon avalanche photo-diodes (APD's) are used for collecting the luminescence signal coming from the NV centers. Multiple lenses, filters, pinholes and irises are used to obtain the desired laser beam. An acousto-optic modulator (AOM) from Crystal Technology, Inc. 3200-146 is used to create the laser pulses. The sample is mounted onto a PI PZT-Flexure Stage P-517K023. Three different objectives, an Olympus LMPlanFL N 100x /0.80 ∞/0/FN26.5 air objective, an Olympus UPlanSApo 40x/0.95 ∞/0.11-0.23/F26.5 air objective and a JAPAN UPlanSApo 60x/1.20W ∞/0.13-0.21/FN26.5 water objective are used during the measurements. As a microwave source, a digital attenuator TEA4000-7 from Telemakus is used. The MW pulses are created using microwave switcher ZASWA-2-50DR+ DC-5 GHz from Mini-circuits and the signal is then amplified with Mini-circuits amplifier model ZHL-16W-43-S+. For the pulsed-measurements, a pulse card was installed in the set-up and was used to control the AOM and the MW switcher. This enabled us to develop specific pulse protocols needed for the different pulsed-measurements.
A schematic representation of the set-up used during the measurements is depicted in figure 9.

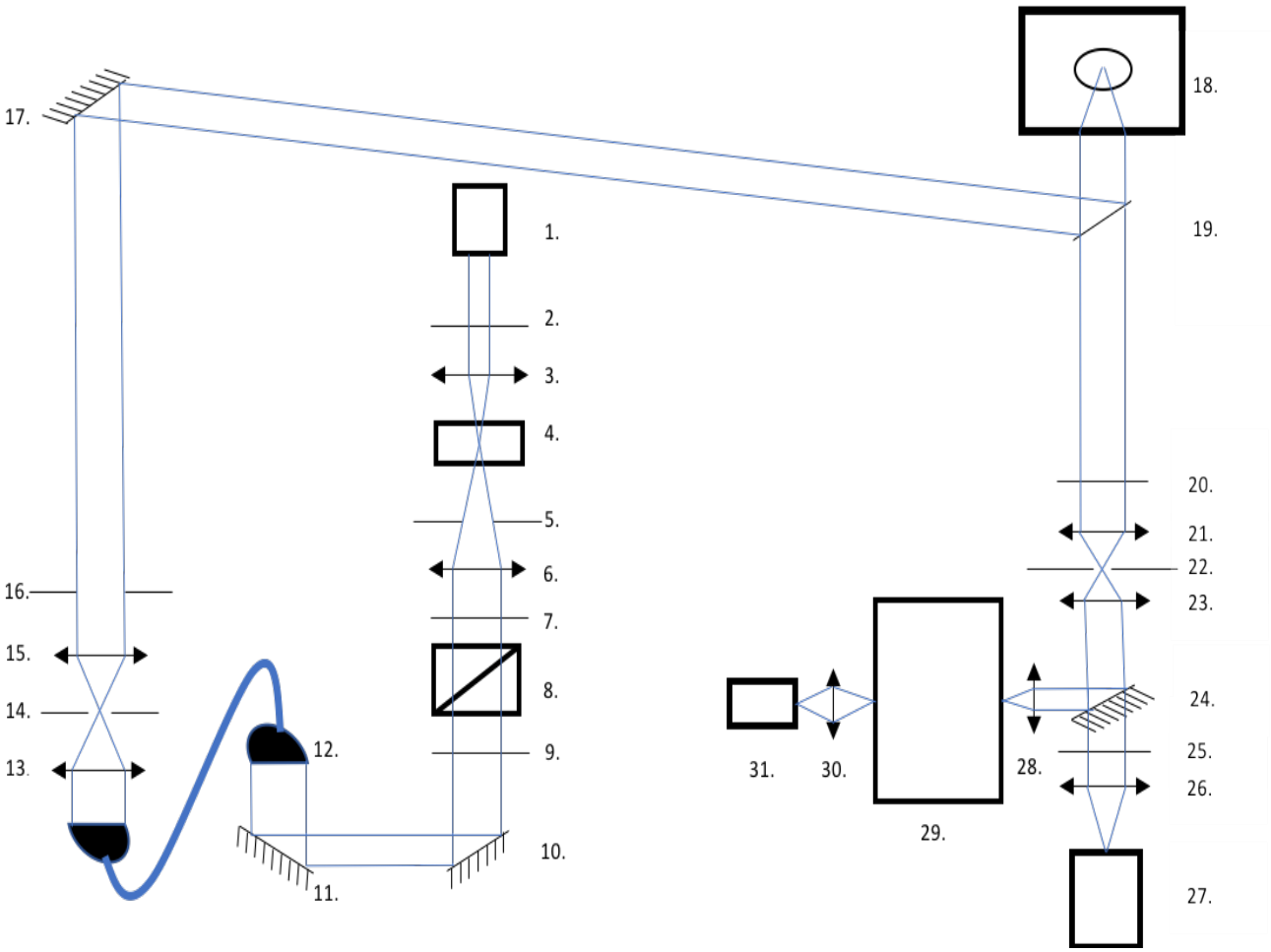

Figure 9: Schematic representation of the home built confocal microscope set-up. 1. Green laser source – 2. Neutral density filter – 3. Lens 150 mm – 4. AOM – 5. Iris – 6. Lens 150 mm – 7. ½ wave plate – 8. Polarizing beam-splitter – 9. laser line filter – 10. Mirror – 11. Mirror – 12. Single mode fiber – 13. Lens 30 mm – 14. Pinhole 200 mm – 15. Lens 150 mm – 16. Iris – 17. Mirror – 18. Piezo stage with sample holder (mirror and objective on z-stage)– 19. Dichroic mirror – 20. Filter LP 550 nm – 21. Lens 100 mm – 22. Pinhole 25 µm – 23. Lens 100 mm – 24. Removable mirror – 25. Filter wheel – 26. Lens 40 mm – 27. APD on x,y,z stage – 28. Lens 50mm – 29. Monochromator – 30. Lens 30 mm – 31. Detector

ODMR measurements

Dried sample

NDs were dissolved in milliQ water with a concentration of 300 µg/ml. A droplet of 50 µl was placed on the sample holder and dried in the air. First ODMR measurements were performed on a dried ND sample. Microwaves were applied to the sample via an omega-shaped antenna. In a second sample, the omega-shaped antenna was replaced by a wire mounted to the printed circuit board (PCB). The laser power as well as the microwave power were varied to obtain the best contrast (as discussed in the result part). A step size of 1 MHz, integration time of 100 ms and 20 iterations were used. Measurements were performed on three different spots, each with a different number of counts (0.168, 2.25 and 23 million counts). During the measurements, an air objective with N.A. of 0.80 was used. Data were fitted by using Origin and employing a double Lorentzian function:

$$y = I + \left(\frac{A_1 * W^2}{(F - F_0 - Asp)^2 + W^2}\right) + \left(\frac{A_2 * W^2}{(F - F_0 + Asp)^2 + W^2}\right)$$

Liquid measurements

For the liquid measurements, a special sample holder was designed (see figure 10). The nanodiamonds were suspended in milliQ water (following the same procedure as for the dried sample). Two concentrations were used (300 µg/ml and 600 µg/ml). A drop of 50 µl solution was brought on the sample holder, in the middle of the wire. Again, laser and microwave power were varied to obtain best contrast. To delay the evaporation of the droplet, a small cap was placed upon the cover glass. Three different objectives were used for measuring the ODMR spectra; an air objective with a N.A. of 0.80, an air objective with an N.A. of 0.95 and a water objective with an N.A. of 1.20. The same parameters as for the dried sample measurements were used: a step size of 1 MHz, integration time of 100 ms and a mean number of iterations of 20.

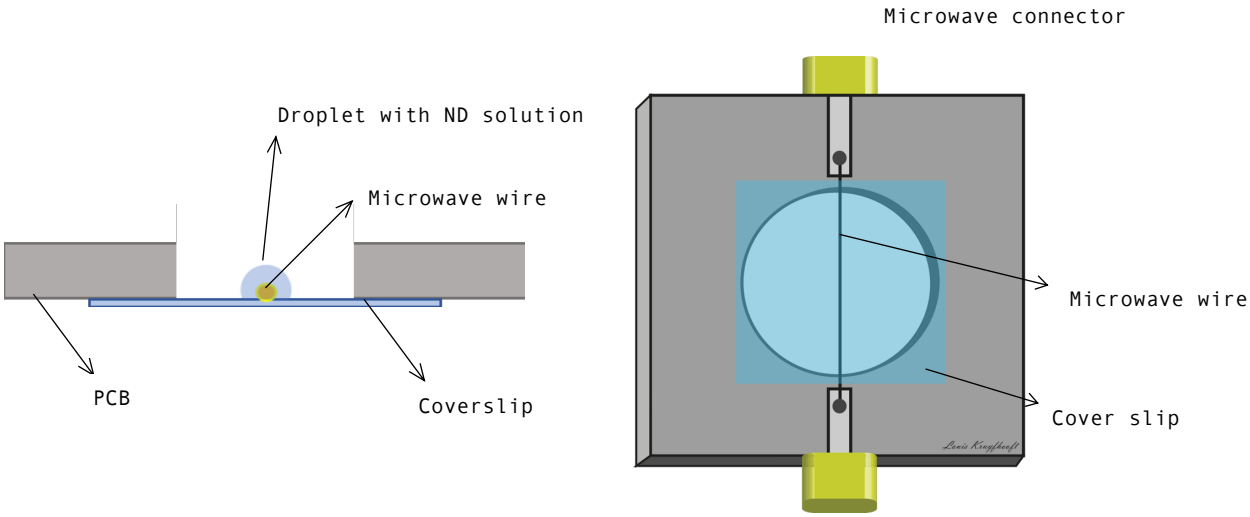

Figure 10: Sample holder constructed for ODMR measurements of NDs in liquid. (side- and top view)

Pulsed measurements

Rabi measurements

Single crystal:

To test the developed pulsed-ODMR sequences, I first performed Rabi nutations on a single crystal diamond sample. For the measurements, a pulsed laser and MW sequence was used (see chapter Pulsed-ODMR). However, the same laser pulse was used for both, NV initialization and NV spin readout. An external magnetic field, using a magnet, was applied to split the resonances. The two resonances were measured via CW-ODMR corresponding to the ground state transition of the m_s =0 and m_s = -1 spin states or of the m_s =0 and m_s = +1 spin states. The laser and MW power were varied to obtain the best ODMR contrast (0.1 mW – 0.9 mW for laser power, 4 W – 14 W for MW power). One of the MW frequencies at which the ground transitions occur was chosen to proceed with Rabi measurements. Two sets of Rabi measurements were performed. One at the resonance frequency, and one at off-resonance frequency that doesn't induce spin excitation and the Rabi graph was plotted as function of contrast with respect to the duration of MW pulse. Contrast was calculated using following equation:

$$\frac{Luminescence\ off\ resonance - Luminescence\ on\ resonance}{Luminescence\ off\ resonance} * 100$$

Optimization of Rabi, in terms of the pulse scheme used, were mainly obtained by varying the laser pulse duration. For the measurements an air-objective with a numerical aperture of 0.95 was used. Result of the measurement is a sinusoidal graph, which represents the Rabi – oscillations. Data were fitted in Origin using following equation:

$$y = -A * \cos\left(2 * pi * \frac{t + tPh}{Trab}\right) * e^{-\frac{t}{T2s}} + B * e^{-\frac{t}{T2s}} + C * t + D$$

Nanodiamonds:

Rabi measurements on the dried ND sample were performed using the same protocol as for the single crystal measurements. Since the NV-axes are oriented randomly, no external magnetic field was applied. The used MW frequencies were based upon one of the two peaks which result from zero-field splitting. Two different objectives were used, an air-objective with a numerical aperture of 0.95 and a water-objective with a numerical aperture of 1.20. A droplet of 50 µl was placed on the sample holder and dried in the air.

T1 measurements

Single crystal:

First T1 measurements were performed on a single crystal diamond sample. The π-pulse (laser pulse duration at which the electrons are switched between the bright and the dark state) was extracted from Rabi measurements. Once again, the same laser pulse was used to initialize and readout the NVs. Laser and MW intensity were varied to achieve highest contrast. 200 iterations were used together with integration time of 100 ms. An air-objective with a numerical aperture of 0.95 was used. As a pulse scheme, the MW-pulse was fixed at the pi-pulse. Laser pulse length was at 1000 ns. The delays between laser pulse and MW pulse was set at 300 ns. The τ-value (time between MW- and laser-pulse) increased with a fixed value to obtain the T1 decay. The contrast was calculated using the same formula as for the Rabi measurements. Data were fitted in Origin using following equation:

$$y = A_1 * e^{-\frac{x}{t_1}} + y_0$$

Nanodiamond particles:

T1 measurements on the dried ND sample were performed using the same protocol as for single crystal diamond. A water objective with a numerical aperture of 1.20 and an air objective with a N.A. of 0.95 were used. Laser pulse lengths of 2000 and 2500 ns were tested. The delay between laser pulse and MW pulse were kept at 300 ns.

Results & Discussion

CW-ODMR spectra

Dried nanodiamond sample on a cover slip

The first ODMR measurements, to master the measuring techniques, were performed on a dried ND sample with omega-shaped MW antenna using an air-objective with a NA of 0.80. Microwave (MW) power and laser power were varied (MW power from 0.4 to 8 W, laser power from 0.02 to 0.7 mW) to obtain best conditions for ODMR measurements. Three different spots (spot 1, spot 2, spot 3 – see figure 11) from multiple NV in focus (spot 1: ~20, spot 2: ~95) to single NV in focus (spot 3) were examined. (See figure 12).

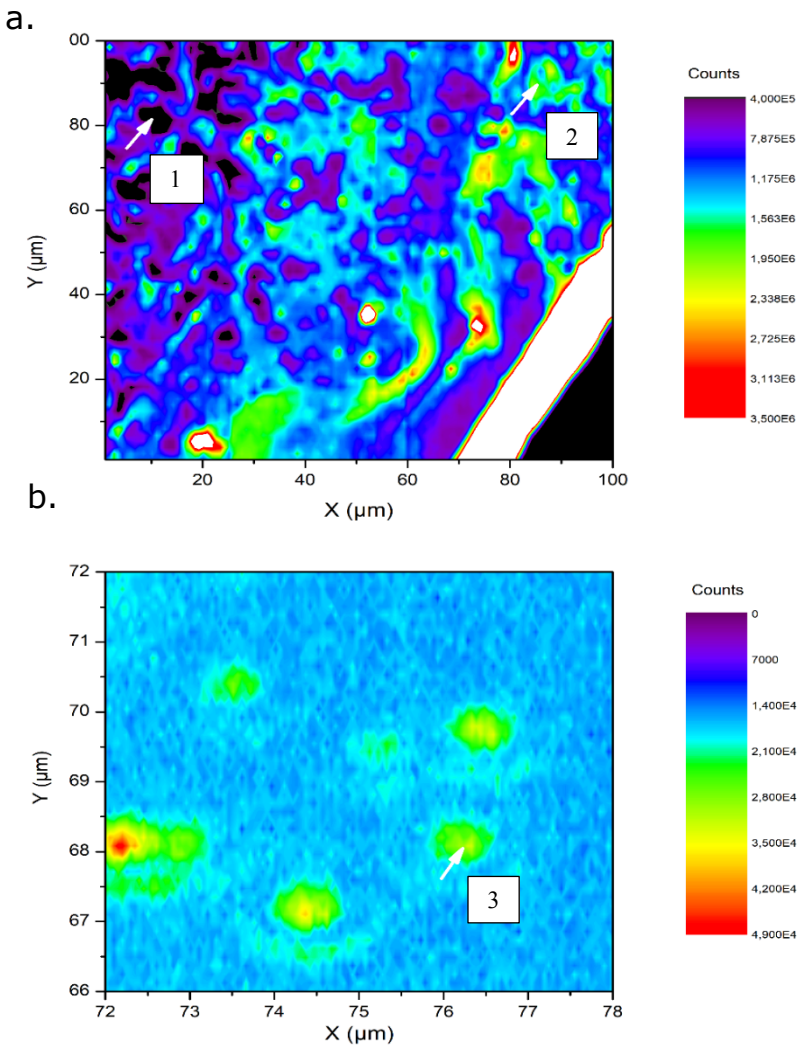

Figure 11: Luminescence confocal map of the three different spots where the ODMR spectra were measured. A. Spot 1 – 380 000 counts (left) and spot 2 - 1 930 000 counts (right) are indicated with the white arrows. B. Spot 3 (15 000 counts) is indicated with the white arrow.

Spot 1: 380 000 counts

a.

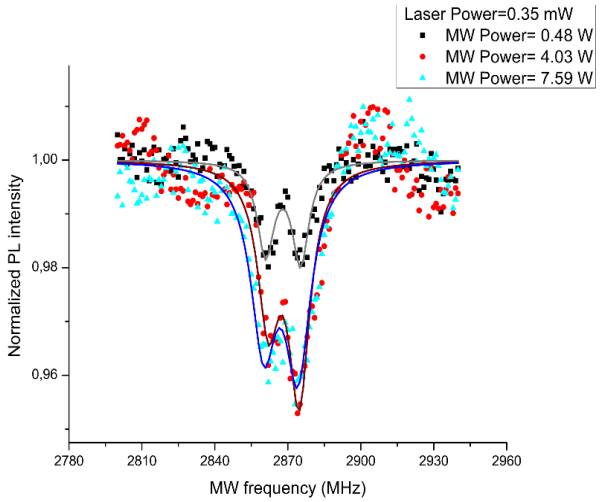

b.

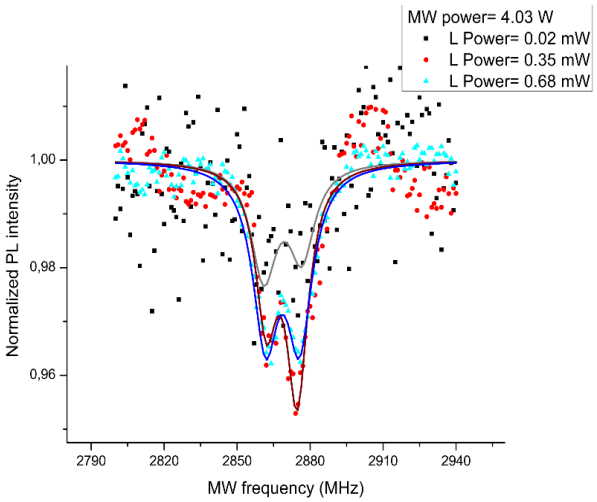

Spot 2: 1 930 000 counts

c.

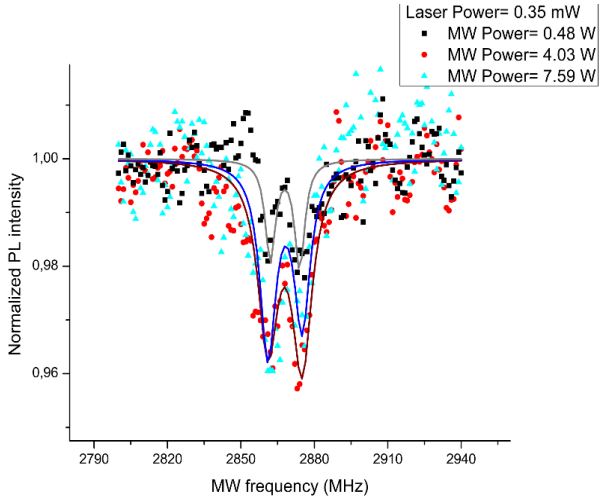

d.

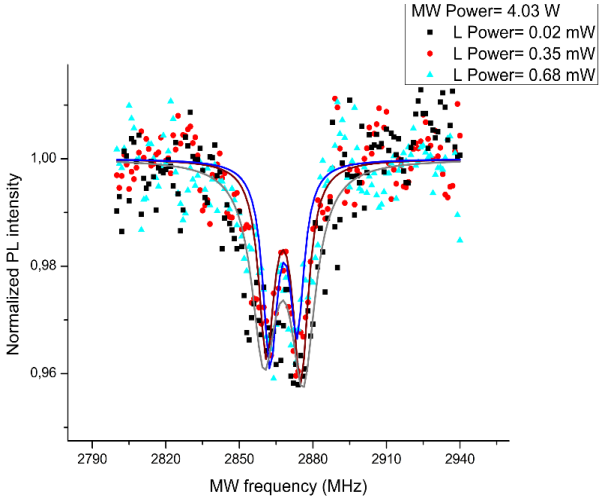

Spot 3: 15 000 counts

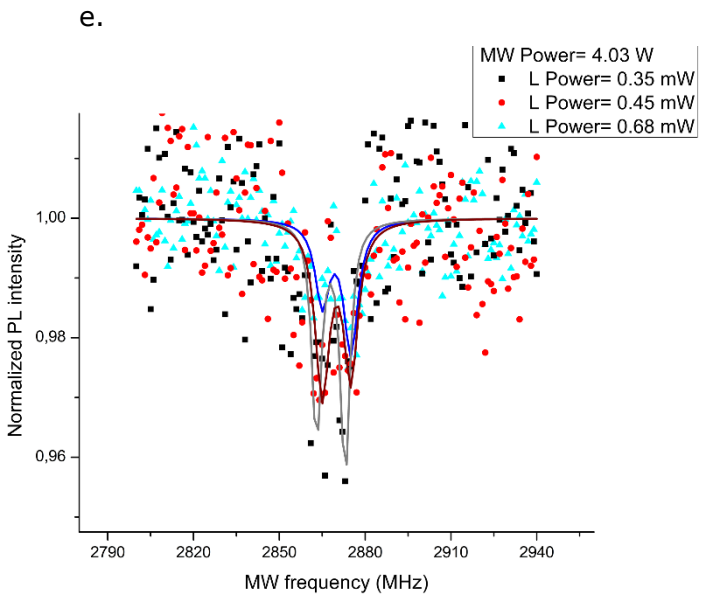

Figure 12: ODMR spectra of ND's dried on surface measured on three different spots. Multiple MW and laser (L) powers are used. A. ODMR spectrum at spot 1 with constant laser power and variable MW power. B. ODMR spectrum at spot 1 with constant MW power and variable laser power. C. ODMR spectrum at spot 2 with constant laser power and variable MW power. D. ODMR spectrum at spot 2 with constant MW power and variable laser power. E. ODMR spectrum at spot 3 with constant MW power and variable laser power.

Successful ODMR spectra were obtained from the ND particles dried on the sample holder. Three measurements for each spot were performed with increasing laser- and constant microwave power and the other way around. It can be noticed that for a different number of NVs in focus, the optimal laser power varies. For higher number of NVs I got better results with higher laser power. For single NV measurement lower laser power is sufficient to saturate the NV signal and additional increase of the laser power only introduces noise in the system.

When the laser power is kept constant and the MW power is varied, we see for spot 1 and 2 that contrast increases for the higher MW power, however too high MW power won't benefit anymore in increased contrast but will cause power broadening, which means that due to higher MW- power the peaks becomes broader, which leads to a shorter coherence time. I have optimized the CW-ODMR contrast by determining the optimal laser and MW power and determined the properties of the ODMR spectra (contrast, full width at half maximum, zero-field splitting). This information was used for measurements in liquid.

In liquid

Since the final goal is to measure inside cells, ODMR measurements had to be performed in liquid. Three different objectives (two air- and one water-objective), each with a different numerical aperture (NA 1 – 1.2) were used. The PL signal depends on the number of NV centres in the confocal volume in time. When the NV centre concentration is too small, too few NV centers will be taken into the spectrum, resulting in a decrease in PL intensity. However even for a single NV centre, ODMR can be measured. When an ND aggregate enters the confocal volume, this will result in a large increase in luminescent counts. Too high number of NV centres in the confocal volume results in lower MR contrast. Another reduction of MR contrast results from the diffusion of NDs from the confocal volume together with the drift of some NDs far from the MW antenna. Two different ND-concentrations were used (300 µg/ml and 600 µg/ml). Best results were obtained with the high ND-concentration of 600 µg/ml using the air-objective with a N.A. of 0.80 and a water-objective with a N.A. of 1.20. (See figure 13).

To collect the most signal, I made sure that the measurements were performed inside the liquid by bringing the whole confocal volume inside the water droplet. Due to some outliers, together with ND particle movement and aggregates moving through the confocal volume, spikes in the signal were observed, resulting in a "disturbed" ODMR spectrum. However, an ODMR signal was still clearly visible. These were the first succeeded ODMR measurements in liquid at IMO.

Air objective 1 (N.A.: 0.80 – ND concentration of 600 µg/ml):

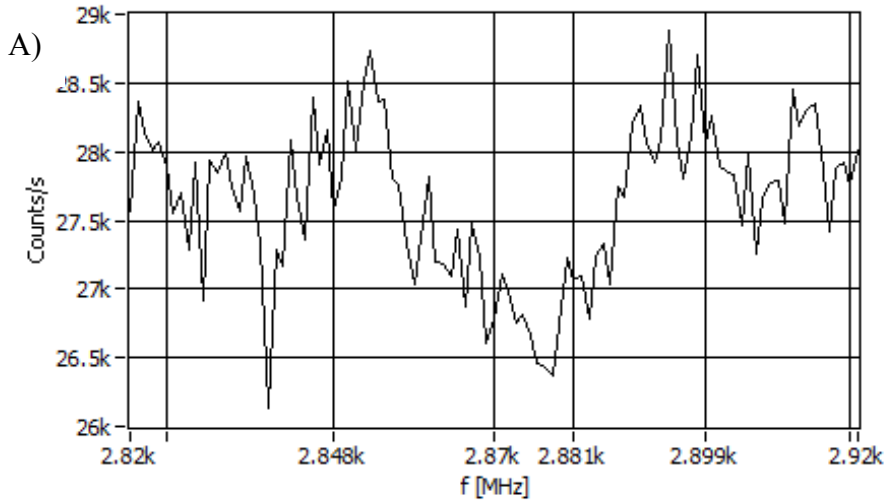

Water objective (N.A.: 1.20 – ND concentration of 600 µg/ml):

B)

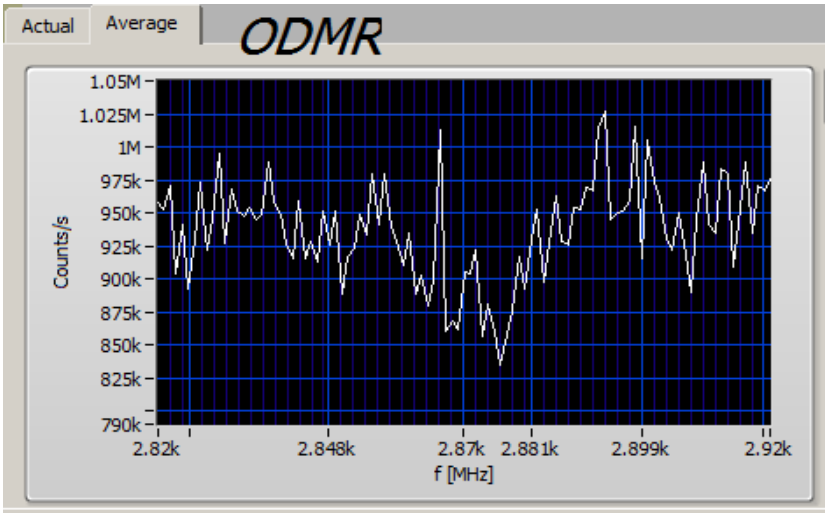

Figure 13: Best obtained ODMR spectra from ND particles dissolved in milliQ water (600 µg/ml). A) ODMR spectrum obtained using an air-objective with a N.A. of 0.80. B) ODMR spectrum obtained using a water-objective with a N.A. of 1.20.

Pulsed-ODMR spectra

To enable pulsed-ODMR measurements, installation of a pulse card in the set-up was necessary. Via the pulse card, the AOM and MW switcher can be controlled to obtain specific pulse protocols needed for the pulsed measurements. Since, in the beginning, it was impossible to use the APD for the read-out of only a specific part of the laser pulse, the same laser pulse was used for both initialization and readout of the NV centers. To optimize the signal from the pulsed-ODMR measurements, the pulse protocols were first tested on single crystal diamond. The pi-pulse was obtained from Rabi-oscillation measurements, after which this pulse was used in T_1 relaxation measurements.

Rabi nutations

Single crystal

First Rabi-oscillation measurements were performed on a single crystal diamond sample. The sample consists of a diamond with high concentration of NV centres, mounted on a PCB. Printed antennas were used for MW excitation. Zeeman splitting was obtained by positioning a magnet above the sample using a small plastic
spacer. During these measurements an air-objective with a N.A. of 0.95 was used. A small external static magnetic field was applied to induce Zeeman splitting. On figure 14, the black arrow indicates the spot where the Rabi measurements (A and B) are performed. The ODMR spectrum is depicted in figure 15. Measurements were performed using the MW frequency where the m_s=0 to m_s=+1 transition occurs. Best results were obtained;

- Using a laser pulse duration of 800 ns, and a MW delay of 200 ns. The laser intensity was set at 1 mW and the MW intensity at 5W (Figure 16).
- Using a laser pulse duration of 1200 ns, and a MW delay of 200 ns. The laser intensity was set at 1 mW and the MW intensity at 5W (Figure 17).

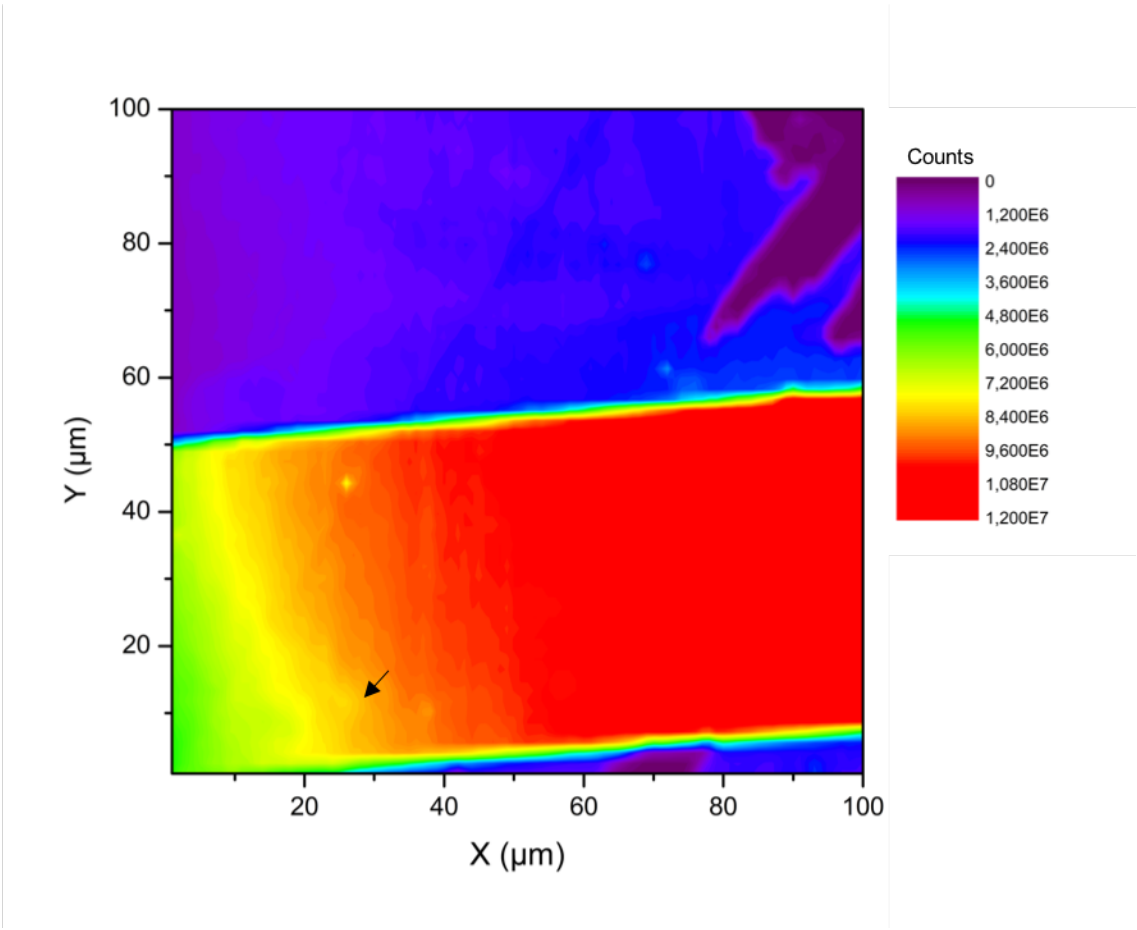

Figure 14: The black arrow indicates the spot on the single crystal diamond, where the Rabi measurements (A,B) took place.

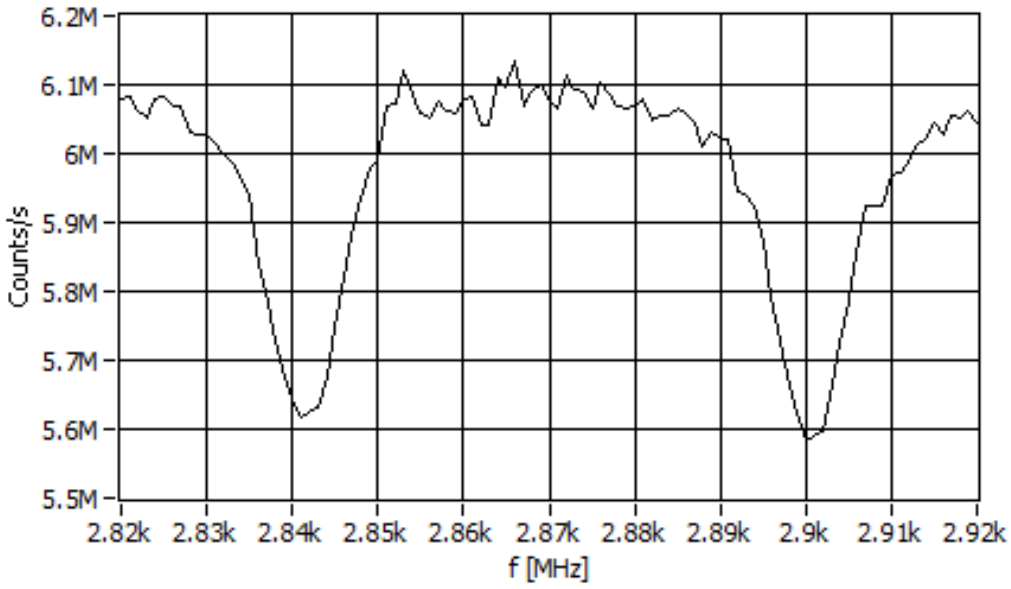

Figure 15: The ODMR spectrum obtained after applying an external magnetic field. The MW frequency where the ms=0 to ms=+1 transition occurs is used for the Rabi measurements A and B.

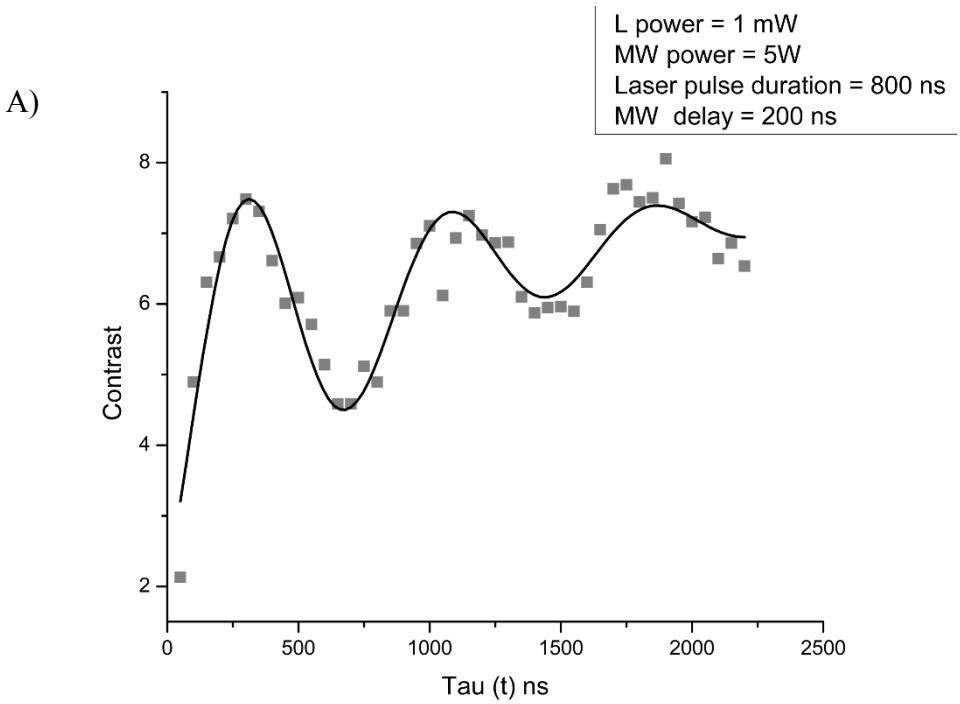

Figure 16: Rabi-oscillation measurements with a laser power of 1 mW, a MW power of 5W, laser-pulse duration of 800 ns and a MW delay of 200 ns.

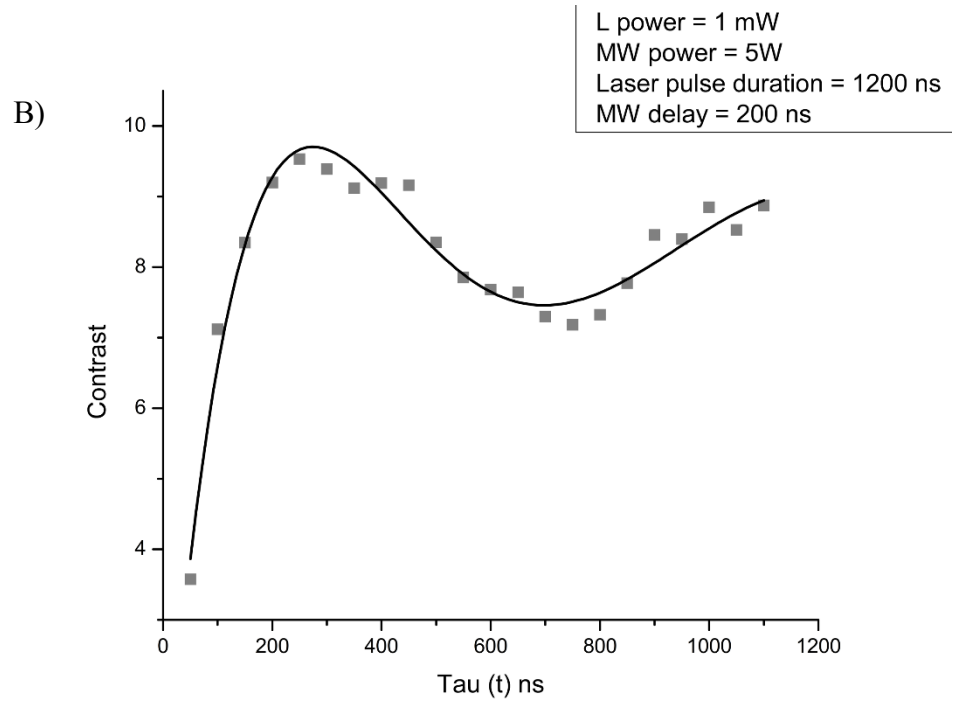

Figure 17: Rabi-oscillation measurements with a laser power of 1 mW, a MW power of 5W, laser-pulse duration of 1200 ns and a MW delay of 200 ns.

To save time, not all Rabi measurements were carried out for as long. Comparing figure 16 and figure 17, we see that an increase in laser pulse duration results in a higher contrast. However, the sinusoidal shape of the obtained graphs wasn't that perfect. Multiple measurements were performed, each with different parameters of the pulse scheme (laser pulse duration and delays) and intensity of the laser or MW, to improve the signal to noise ratio and find the optimal parameters. From the results we see that an increase in laser power did result in higher contrast measurements (figure 20). Too high laser powers however, lead to more noise in the system. Changing the laser pulse duration also let to changes in MR contrast. Generally, we can say that a longer laser pulse is necessary to initialize all NV centres, and thus results in a higher contrast measurement (see figure 21), but it cannot be too long because this will not only bring noise in the system but the occupation of m_s= 0 level returns to steady state population and therefore the contrast will decrease again. For the Rabi measurements the optimal laser pulse duration of 800 ns to 1200 ns, see figure 21, were selected and the measurements were then performed on the same spot. In figure 18 the spot where the Rabi measurements of graph C were obtained is depicted with a black arrow. Looking at the ODMR spectrum, the MW frequency where the ms=0 to ms=+1 transition occurs is used for the Rabi measurements in C. The contrast hasn't change significantly when the laser pulse was increased with 200 ns. The red line graph (figure 21) was taken on a slightly different spot. This may have a small influence concerning the contrast, however the increase in contrast is too high to be only depicted to the measurement on another spot. The longer laser pulse duration (1200 ns) resulted in higher contrast of the Rabi oscillations. Unfortunately, no map and ODMR spectrum from figure 21 were saved. Rabi oscillation measurements on single crystal were successfully accomplished. The pulse scheme parameters were optimized and can now be applied on NDs (see next chapter).

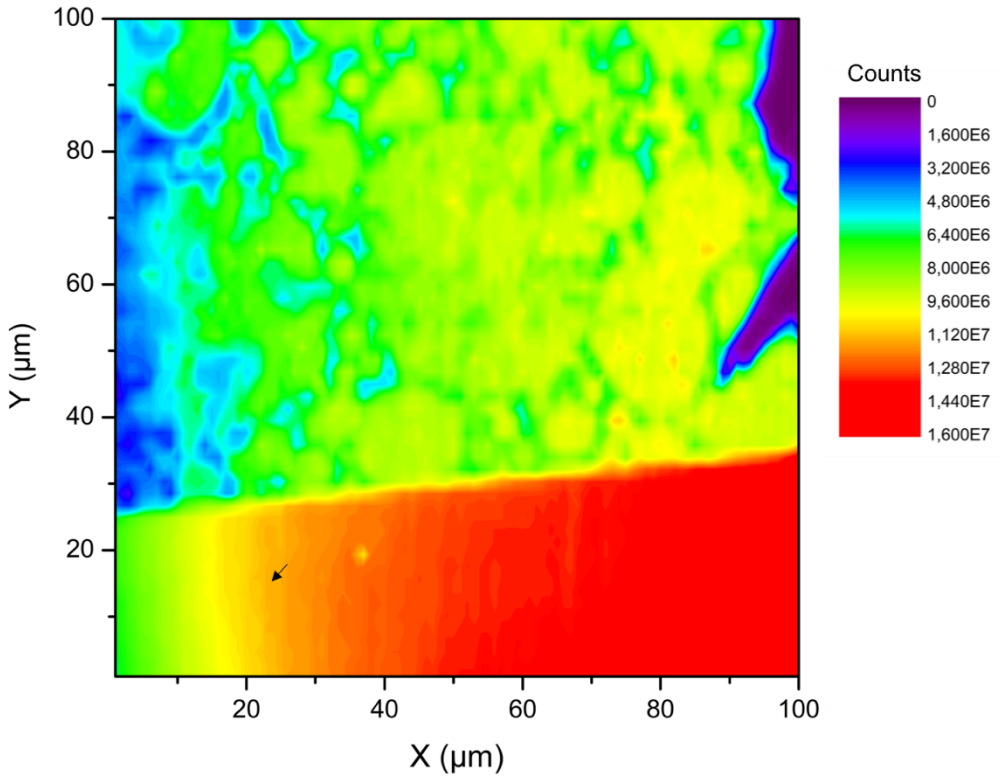

Figure 18: The black arrow indicates the spot on the single crystal diamond, where the Rabi measurements (C) took place.

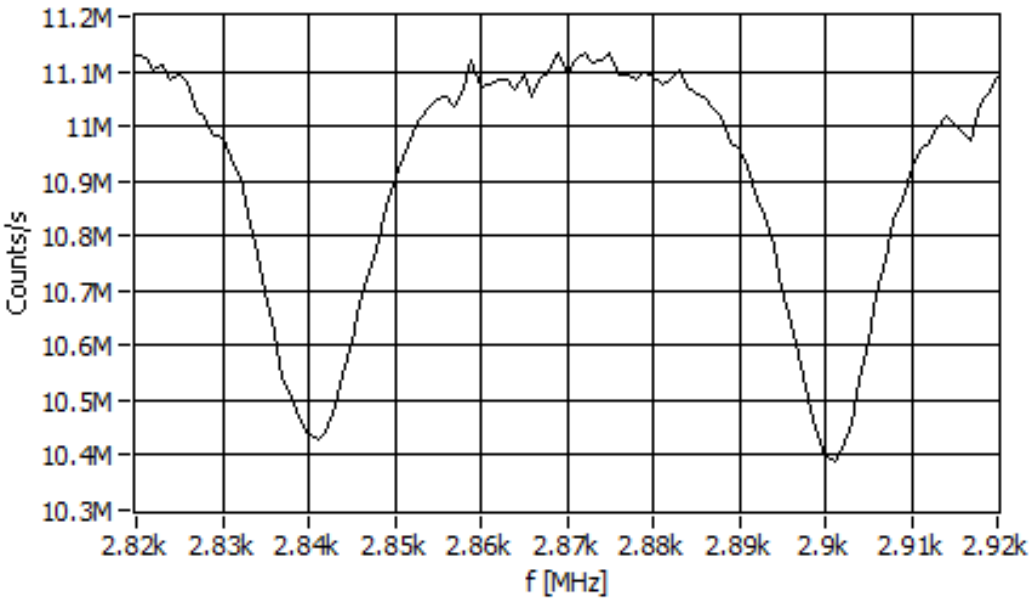

Figure 19: The ODMR spectrum obtained after applying an external magnetic field. The MW frequency where the ms=0 to ms=+1 transition occurs is used for the Rabi measurements in C.

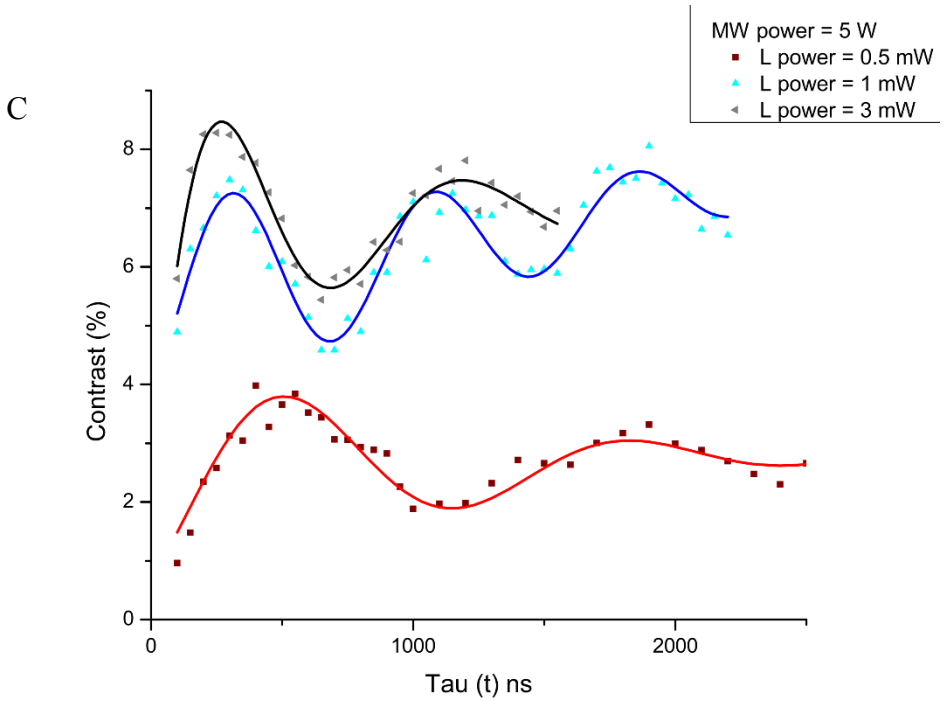

Figure 20: Rabi measurements performed with increasing laser power (0,5 mW; 1 mW; 3 mW) . The other parameters were kept constant at a MW power of 5 W, a laser pulse duration of 800 ns and a MW delay of 200 ns.

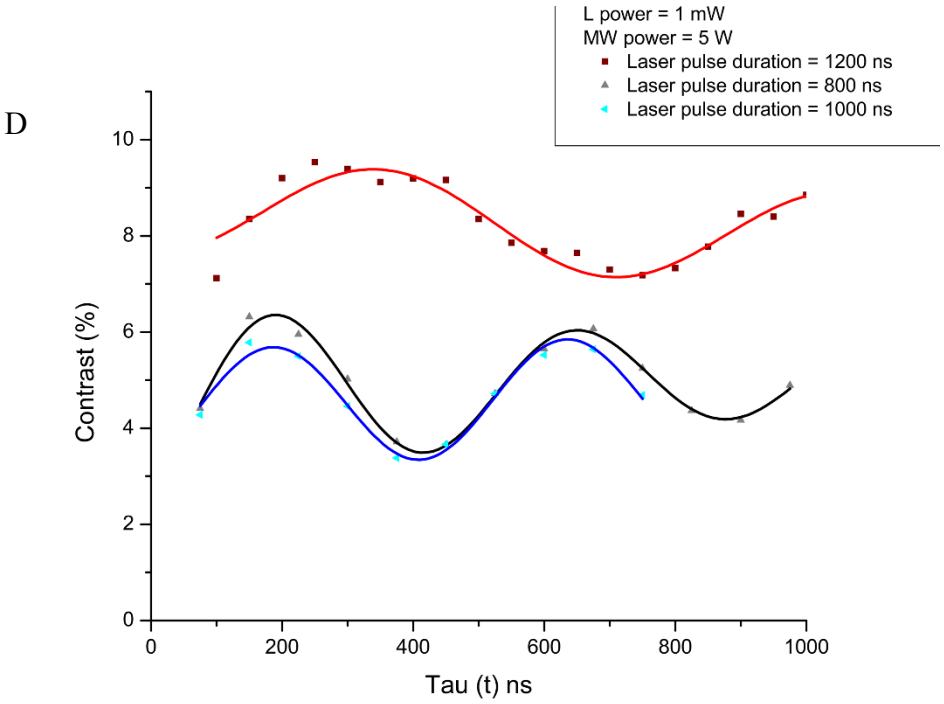

Figure 21: Rabi measurements performed with increasing laser pulse duration (800 ns; 1000 ns; 1200 ns). The other parameters were kept constant at a Laser power of 1 mW, MW power of 5 W and a MW delay of 200 ns. The red graph has been obtained from a slightly different spot.

Nanodiamond particles

A next step were the Rabi-measurements on ND particles. Due to the random orientation of the particles, Zeeman splitting using an external magnetic field was difficult to achieve, as the Zeeman splitting is NV centre axis orientation dependent. During the measurements, two different objectives were used, an air-objective with a numerical aperture of 0.95 and a water-objective with a numerical aperture of 1.20. The spots where the Rabi-oscillation measurements were performed are depicted by a black arrow in figure 22 and figure 26. The ODMR spectra are is shown in figure 23 (where transition at which ms=0 to ms=+1 occurs is used for the Rabi measurements) and figure 24 (where transition at which ms=0 to ms=-1 occurs is used for the Rabi measurements). The resonant frequency was determined using a fitting program.
Best results were obtained;

- Using the air-objective and applying a 1 mW 2000 ns laser-pulse together with a 8 W MW-pulse with a delay of 300 ns (Figure 24).
- Using the water objective and applying a 1 mW 2500 ns laser-pulse together with a 8 W MW-pulse with a delay of 300 ns (Figure 25).

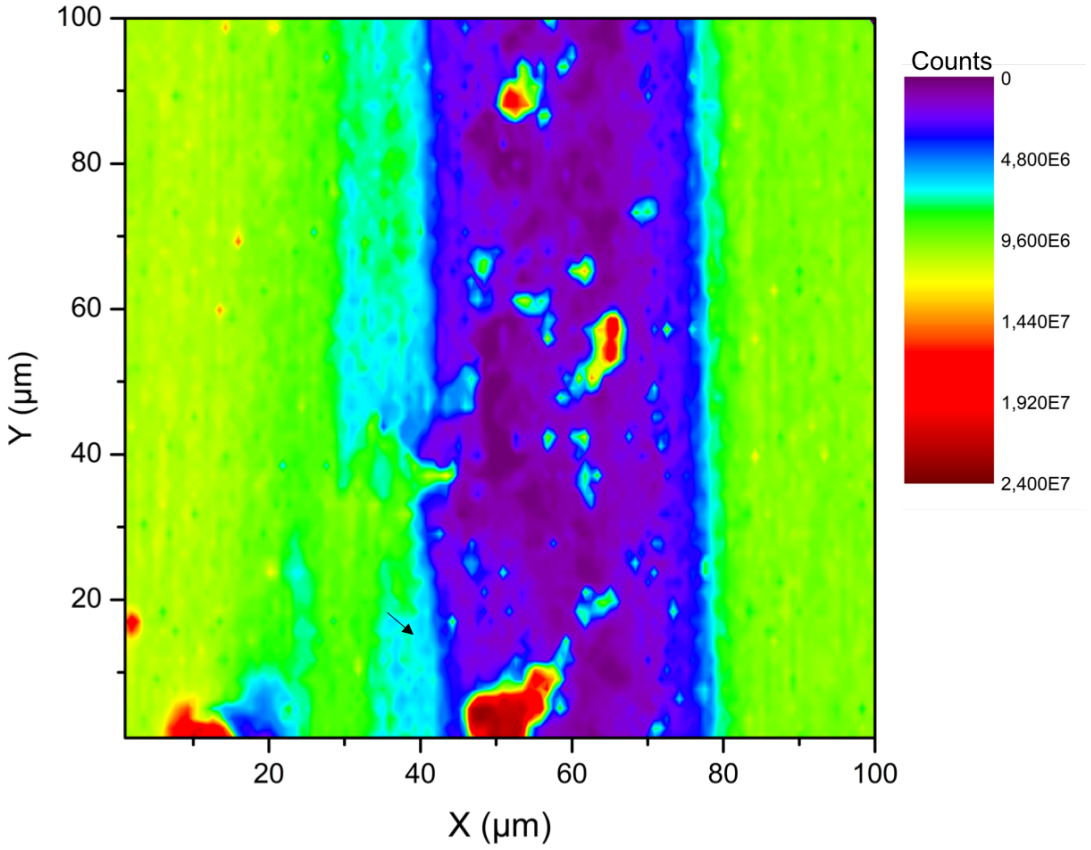

Figure 22: The black arrow indicates the spot on dried ND sample, where the Rabi measurements (E) took place.

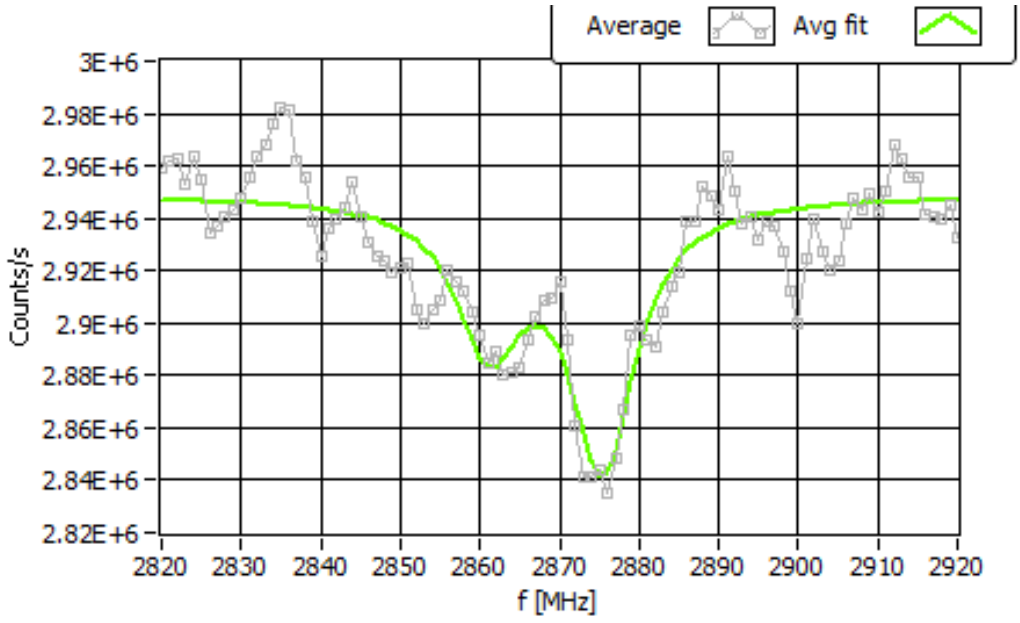

Figure 23: The ODMR spectrum obtained after applying an external magnetic field. The MW frequency where the ms=0 to ms=+1 transition occurs is used for the Rabi measurements in E. Fitting is obtained via a double Lorentzian function.

Looking at the Rabi-oscillations obtained from the air objective, a lot of technical noise in the signal can be seen. Additionally, there was a signal drift. During the measurements, it could be stated that the piezo-stage moved sometimes in the x,y, and z direction. This is possibly the reason for the drift in the measurements. In figure 25 a Rabi-oscillation behavior is clearly visible for the shorter times first slope. However, the longer the measurement proceeded, the signal decays due to the short coherence time of NV spins in ND particles. E.g. the Rabi is modulated by the relaxation time. Other measurements with the water objective also resulted in a Rabi-like behavior, however, the contrast dropped significantly (see figure 28). Despite a drop-in contrast, the π-pulse extracted from the Rabi-oscillations remained the same (at 250 ns). This could be related to the movements of the particles, e.g. quantization axis rotation during the measurement.

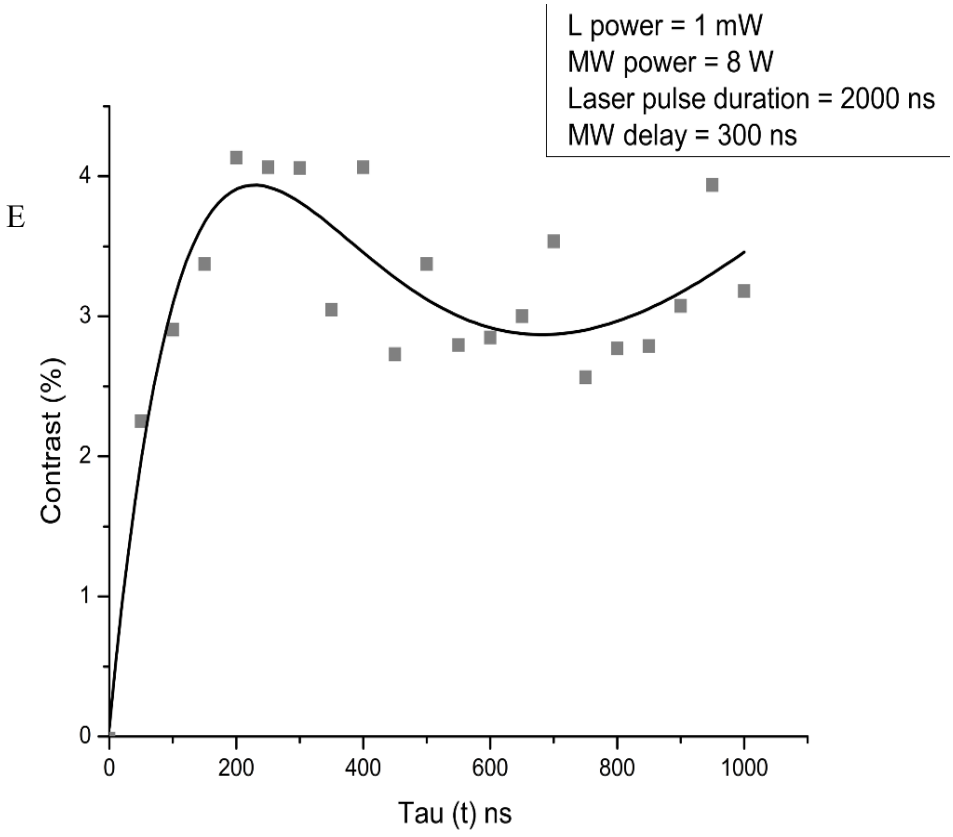

Figure 24: Rabi-oscillation measurements with a laser power of 1 mW, a MW power of 8W, laser-pulse duration of 2000 ns and a MW delay of 300 ns.

As figure 24 and figure 25 are compared to each other, there can again be seen that the π-pulse is situated at around 250 ns. This π-pulse estimate can be considered correct, since in multiple independent measurements the same value shows up.

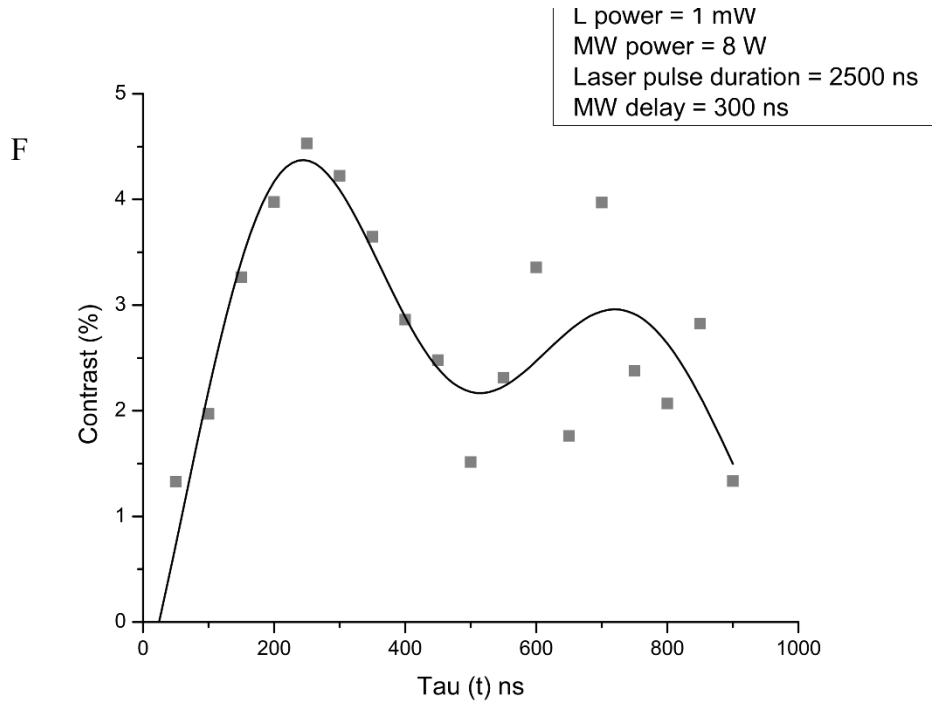

Figure 25: Rabi-oscillation measurements with a laser power of 1 mW, a MW power of 8W, laser-pulse duration of 2500 ns and a MW delay of 300 ns.

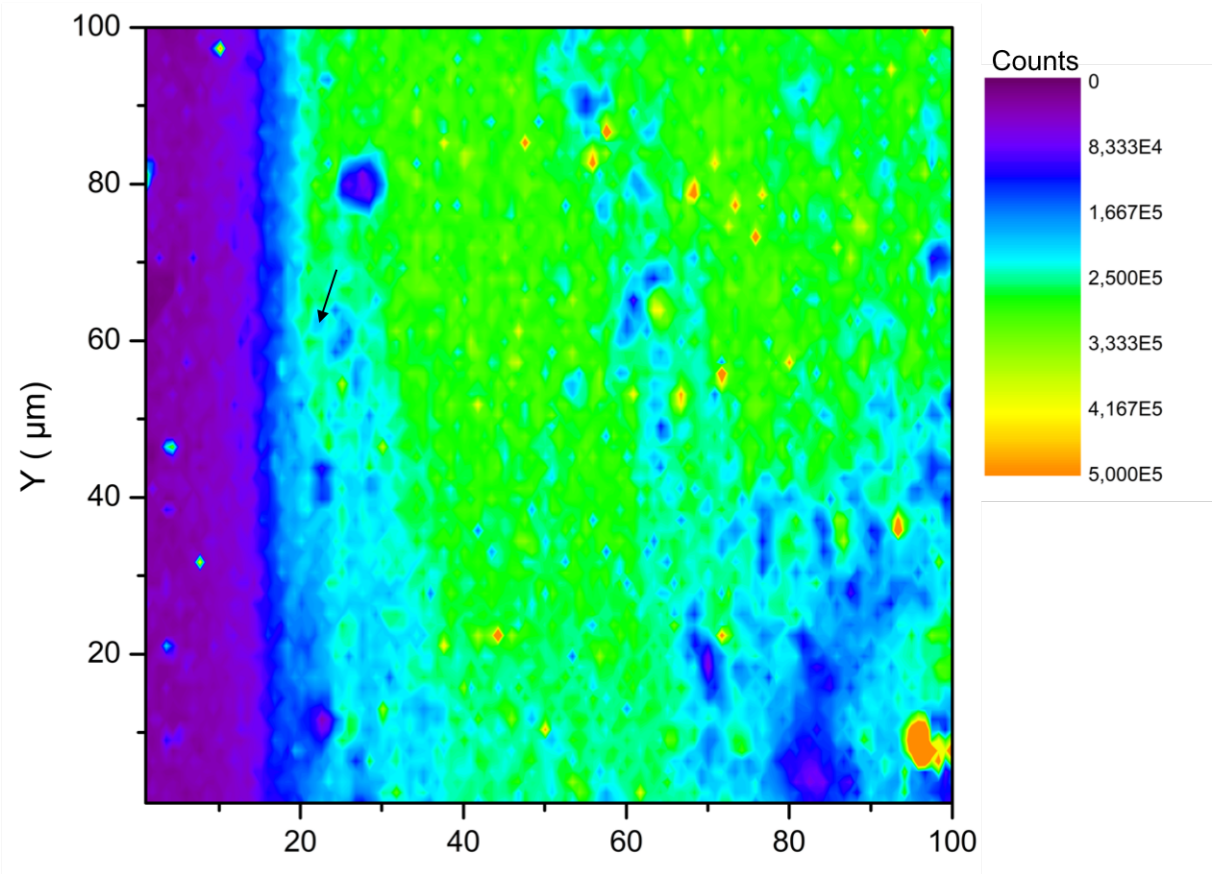

Figure 26: The black arrow indicates the spot on dried ND sample, where the Rabi measurements (F) took place.

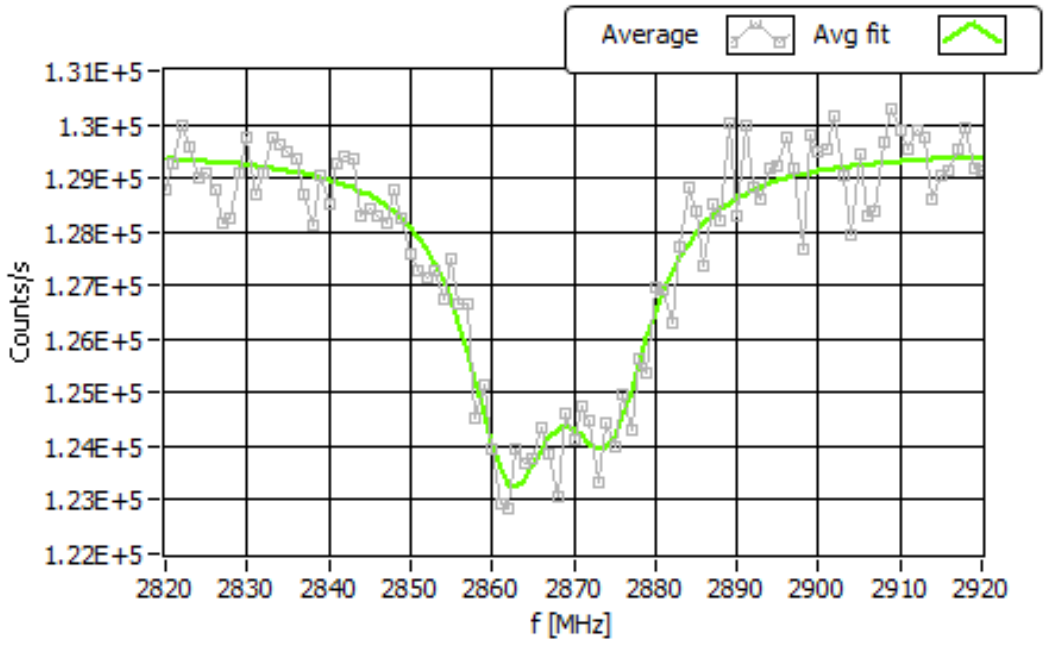

Figure 27: The ODMR spectrum obtained after applying an external magnetic field. The MW frequency where the ms=0 to ms=-1 transition occurs is used for the Rabi measurements in F.

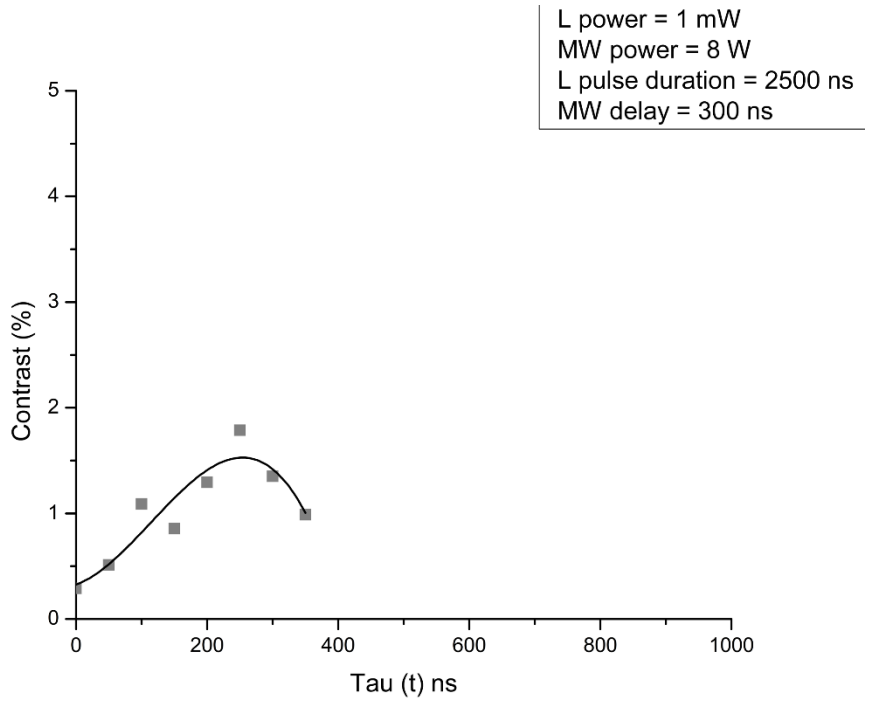

Figure 28: Rabi-oscillation measurements with a laser power of 1 mW, a MW power of 8W, laser-pulse duration of 2500 ns and a MW delay of 300 ns. The contrast dropped significantly compared to figure 15, however the first maximum corresponds to pi/2. From that it can be concluded that the π- pulse remained the same.

Rabi-oscillation measurements on ND particles were successful. It was harder to get a nice signal compared to measurements on single crystal diamond. However, a Rabi behavior could be visualized and parameters were adjusted to obtain the best results. The π-pulse determination for T_1 measurements was harder for ND particle measurements compared to single crystal measurements. However, in both cases, the π-pulse extraction was reliable.

T1 measurements

Single crystal

The pulse protocol for T1, as described previously, was first tested on single crystal diamond. A 3 mW laser-power of 1000 ns and a 5W MW-power was used. The length of the MW pulse was set at 185 ns which was the obtained π-pulse, extracted from the Rabi measurements. The delay of the MW-pulse was set at 300 ns. Looking at figure 29, a decay curve was obtained, which represents the T1 relaxation. After obtaining a successful T1 relaxation measurement, the protocol was proved correct. Next step was to continue with T1 measurements on nanodiamond particles.

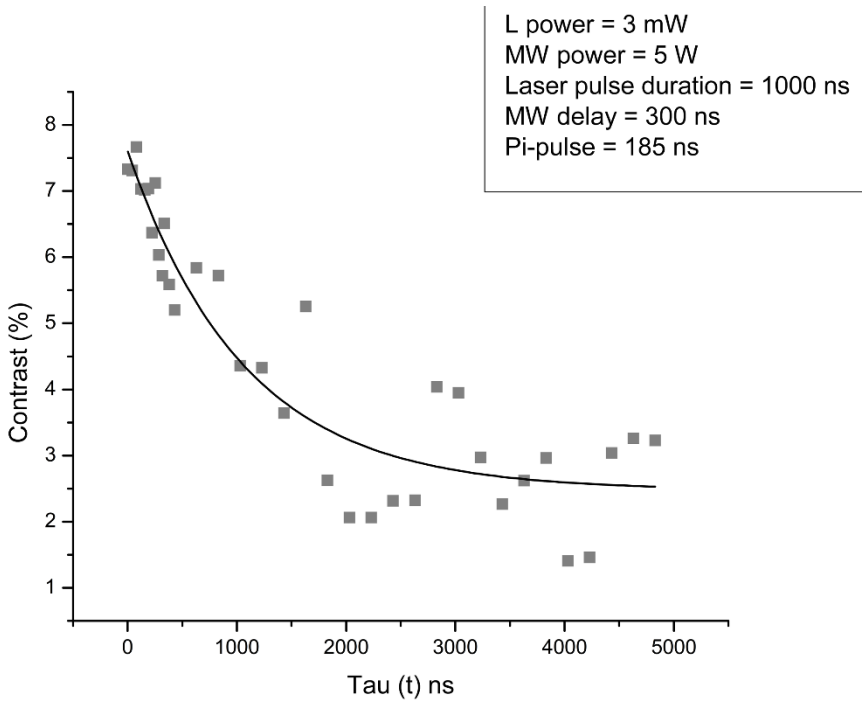

Figure 29: T1 relaxation time on single crystal diamond. Laser power was set at 3 mW, laser pulse duration at 1000 ns. For the MW power, 5W was used. The delay of the MW pulse was set at 300 ns. The π-pulse was 185 ns. The resulting T1 time was 1063 ns obtained from the fit.

Nanodiamond particles

Multiple T1 measurements on nanodiamonds particles were performed. Best results were obtained using a laser power of 1 mW, with a pulse duration of 2000 ns. The MW power was set at 5W with a delay between MW and laser pulse of 300 ns. A 300 ns π-pulse was obtained from the Rabi-oscillation measurement and used as the MW pulse. Looking at the Rabi-measurements described previously, a π-pulse of 250 ns was obtained. However this pulse is also dependent of the spot on the sample where we measured. T1 measurements with a π-pulse of 250 ns where also performed, however with bad results. Looking at figure 30, a decay curve was obtained, representing the T1 relaxation.

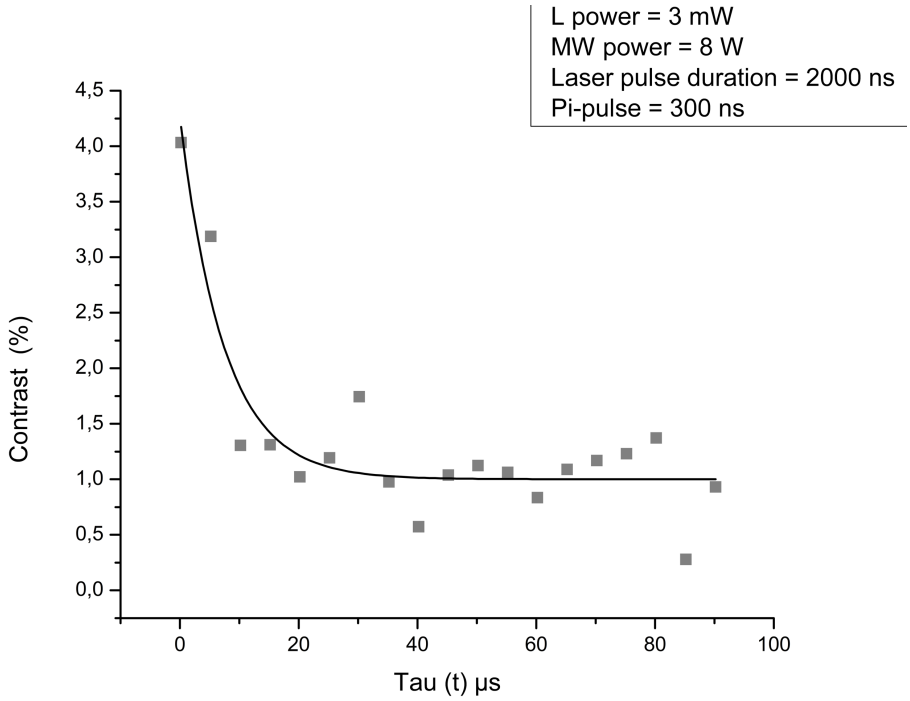

Figure 30: T1 relaxation time on nanodiamond particles. Laser power was set at 3 mW, laser pulse duration at 2000 ns. For the MW power, 8W was used. The delay of the MW pulse was set at 300 ns. The π-pulse was 300 ns. Obtained T1 time is 7,5 μs calculated from the fit.

Previous T_1 relaxation was obtained without gating the APD and following the pulse sequence as explained in the materials & methods part. Changes on the software allowed us to gate the APD shortening the measurement time significantly. New T_1 measurements were performed as demonstrated in figure 31.

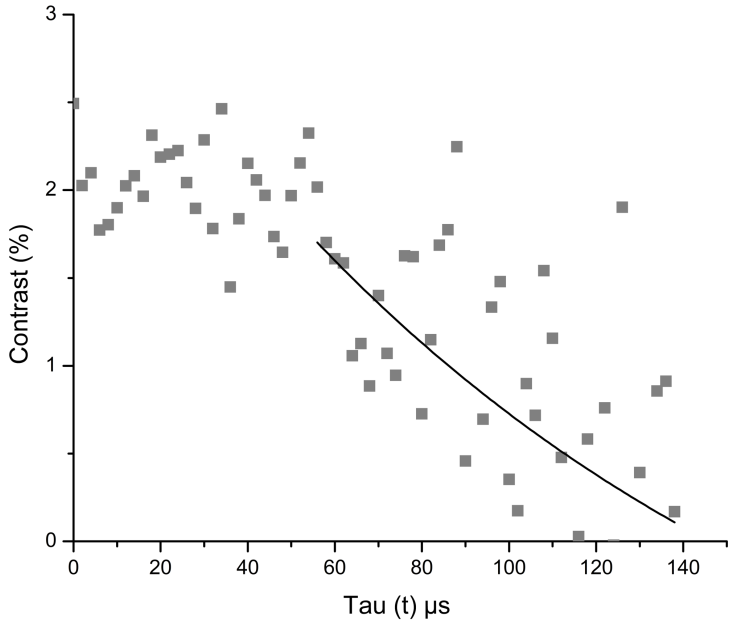

Figure 31: T1 relaxation time on nanodiamond particles using a gated APD. Laser power was set at 0.1 mW, laser pulse duration at 4360 ns. For the MW power, 5W was used. The delay of the MW pulse was set at 320 ns. The π-pulse was 260 ns. Obtained T1 time is 135 μs calculated from the fit.

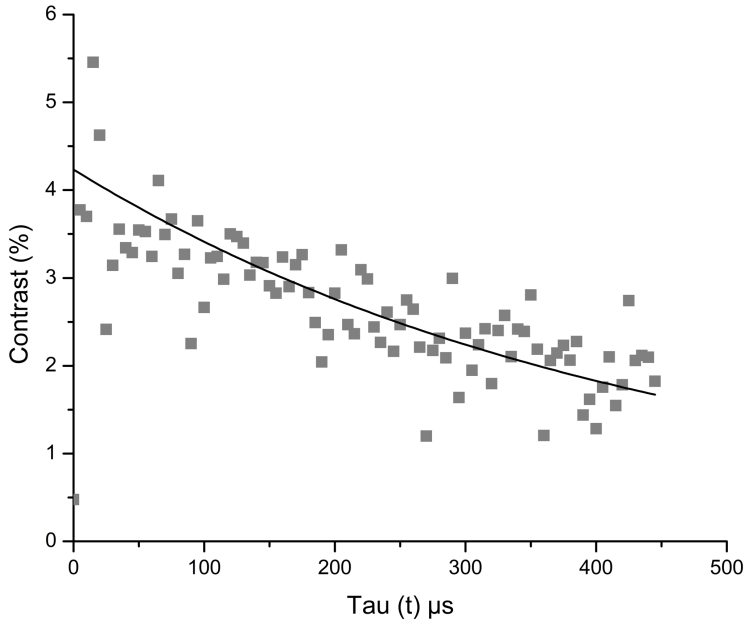

Figure 32: T1 relaxation time on nanodiamond particles after adding nickelsulfate onto the dried nanodiamond sample using a gated APD. Laser power was set at 0.1 mW, laser pulse duration at 4360 ns. For the MW power, 5W was used. The delay of the MW pulse was set at 320 ns. The π-pulse was 260 ns. Obtained T1 time is 435 μs calculated from the fit.

The goal of this thesis was to demonstrate the possibility to use ND particles as a quantum sensor by observing the change in T_1 time when paramagnetic substances in proximity to the NDs. To do this I added a 50 µl droplet of nickel sulfate dissolved in milliQ water onto the dried ND sample. T_1 measurements (see figure 32) started after the droplet dried out.

T_1 measurements were successfully accomplished on ND particles. Using the gated APD, longer T_1 times were obtained. Since we expected T_1 relaxation times of a few hundreds of microseconds, we can conclude that the software using the gated APD was more reliable compared to using a pulse sequence without a gated APD. We also demonstrated that addition of molecules onto the sample made a significant change in T_1 time.

Conclusion and synthesis

In this thesis we have developed methodology for measurements of presence of moieties carrying electronic spins or in general magnetic properties by using NV centre quantum probes. First, we have performed successfully ODMR measurements on single crystal diamond, dried nanodiamond sample and nanodiamond particles in liquid. The own designed sample holder using a coverslip and MW wire did work properly and was used for most measurements throughout the thesis (except for single crystal measurements). We have optimized the parameters of the measurements for measuring a high number of NV centres, specifically a higher laser-power is recommended. For a single NV centre however, a low laser-power is sufficient to obtain a good ODMR. When looking at the MW power, the contrast will decrease when too high powers are applied due to power broadening. However, a sufficient power is needed to obtain good contrast. In liquid ODMR signal was harder to obtain compared to the dried sample. A sufficient high concentration of NDs dissolved in milliQ was necessary to obtain a spectrum. Problems arose due to a moving piezo-stage, which lead to some outliers in the spectrum. Still however, I managed to perform ODMR measurements in liquid for the first time at IMO.

Pulsed-ODMR was first used in Rabi-oscillation measurements on single crystal diamond. Prolonging the laser pulse duration, lead to an increase in contrast. However, too long laser pulses will lead to a decrease in contrast. Dependent on the spot we measured, a different π-pulse was used. Despite these problems, Rabi oscillations were clearly visible. The pulse sequence parameters were optimized in terms of laser power and pulse duration. Hereafter, Rabi-oscillation measurements were performed on ND particles. It was harder to obtain a nice spectrum in comparison to the single crystal diamond. However, a Rabi-like behavior was still clearly visible. Multiple measurements using exactly the same parameters resulted in changes in contrast. Probably the moving piezo-stage and noise in the measuring room may have influenced the results. Yet, the π-pulse remained the same.

After determination of the π-pulse, T1 relaxation measurements were performed on single crystal diamond to test the pulse protocol. First measurements directly showed a decay curve, as expected for T1 relaxation measurements, which proved that the used pulse protocol was correct. Improvements concerning contrast and decay time weren't applied to prevent wasting time and T1 measurements were continued on ND particles. Better results were obtained after hardware optimization, which allowed us for gated APD measurements. Again, a T1 relaxation curve was obtained. The relaxometry decay curves were successfully measured and the T1 times were obtained from the data fit to be 135 μs. Since we wanted to show that adding molecules to the NDs would induce a change in T_1 time, we decided to add nickel sulfate onto the ND sample. Successful T_1 decay was obtained, with a significant difference in time compared to the dried ND sample. Due to a lack of time and technical difficulties, I didn't accomplish T1 measurements on NDs in liquid.

As a future outlook, we want to use the NDs for real time measurements inside cells. But first, Rabi oscillation and T1 relaxation measurements on nanodiamond particles has to be improved. A next step is to measure T1 from ND particles in liquid. If this succeeds, NDs covered with spin traps will be examined.

References

1. **Sarwar, M. R. and Saqib, A.** Cancer prevalence, incidence and mortality rates in Pakistan in 2012. *Cogent Medicine .* 2017, Vol. 4, 1.
2. **Ahmad, R.** Free Radicals and Diseases. *Biochemistry, Genetics and Molecular Biology.* 2016, Vol. 17.
3. **Venditti, P., et al.** Mitochondrial metabolism of reactive oxygen species. *ScienceDirect.* 2013, Vol. 13, 2.
4. **Zhang, J., et al.** ROS and ROS-Mediated Cellular Signaling. *Oxidative medicine and cellular longevity.* 2016.
5. **Brieger, K., et al.** Reactive oxygen species: from health to disease. *Swiss medical weekly.* 2012, Vol. 142, 17.
6. **Dikalov, S.I. and Harrison, D.G.** Methods for Detection of Mitochondrial and Cellular Reactive Oxygen Species. *Antioxidants & Redox Signaling.* 2014, Vols. 372-382.
7. **Li, Y., et al.** In Situ Real-Time Chemiluminescence Imaging of Reactive Oxygen Species Formation from Cardiomyocytes. *International Journal of Biomedical Imaging.* 2008.
8. **Mochalin, V.N., et al.** Adsorption of Drugs on Nanodiamond: Toward Development of a Drug Delivery Platform. *Molecular Pharmaceutics.* 2013, Vols. 10: 3728–3735.
9. **Kucsko, G., et al.** Nanometre-scale thermometry in a living cell. *Nature.* 2013, Vols. 500: 54–58.
10. **Perevedentseva, E., et al.** Biomedical applications of nanodiamonds in imaging and therapy. *Nanomedicine.* 2013, Vols. 8(12): 2041-60.
11. **Prawer, S. and Aharonovich, I.** Quantum Information Processing with Diamond: Principles and Applications. 2014, Vol. 9, 1.
12. **Rendler, T., et al.** Optical imaging of localized chemical events using programmable diamond quantum nanosensors. *Nature Communications.* 2017.
13. **Zhu, Y., et al.** The Biocompatibility of Nanodiamonds and Their Application in Drug Delivery Systems. *Theranostics.* 2012, Vol. 2.
14. **Barnard, A. S.** Predicting the Impact of Structural Diversity on the Performance of Nanodiamond Drug Carriers. *Nanoscale.* 2018.
15. **Beyler-Çiğil, A. and VezirKahraman, M.** Effect of surface modification on nano-diamond particles for surface and thermal property of UV-curable hybrid coating. *Progress in Organic Coatings.* 2016, Vol. 101.
16. **Hui, Y. Y., Cheng, C. L. and Chang, H. C.** Nanodiamonds for optical bioimaging. *Journal of Physics D: Applied Physics.* 2010, Vols. 43-37.
17. **Foxa, K., et al.** Nanodiamond-polycaprolactone composite: A new material for tissue engineering with sub-dermal imaging capabilities. *Materials letters.* 2016, Vol. 185.
18. **Faklaris, O., et al.** Photoluminescent Diamond Nanoparticles for Cell Labeling: Study of the Uptake Mechanism in Mammalian Cells. *ACS Nano.* 2009, Vol. 3(12).
19. **Mochalin, V. N., et al.** The properties and applications of nanodiamonds. *Nature technology.* 2012, Vols. 7: 11-23.
20. **Mildren, R. and Rabeau, J.** Optical engineering of diamond.
21. **Vul, A. Ya., Aleksenskiy, A. E. and Dideykin, A. T.** Detonation nanodiamonds: technology, properties and applications. *Nanosciences and nanotechnologies.* 1, 2009, Vol. 3.
22. **Simakov, S.K.** Metastable nanosized diamond formation from a C-H-O fluid system. *Journal of material research .* 2010, Vols. 25-12.

23. **Kudarenko, I. P., et al.** Detonation Nanodiamond-Assisted Carbon Nanotube Growth by Hot Filament Chemical Vapor Deposition. *Basic solid state physics.* 2017.
24. **Bundy, F.P.** Direct Conversion of Graphite to Diamond in Static Pressure Apparatus. *The Journal of Chemical Physics.* 1963, Vols. 38, 631.
25. **Havlik, J., et al.** Boosting nanodiamond fluorescence: towards development of brighter probes. *Nanoscale.* 2013, Vol. 8.
26. **Rehor, I., et al.** Fluorescent Nanodiamonds Embedded in Biocompatible Translucent Shells. *Small.* 2014, Vols. 1106–1115.
27. **Kohei, M.** Quantum assisted sensing using nitrogen-vacancy (NV) centers in diamond. *AAPPS Bulletin.* 2015, Vols. 25: 12-16.
28. **Felton, S., et al.** Electron paramagnetic resonance studies of the neutral nitrogen vacancy in diamond. *Phys. Rev.* 2008, Vol. 77.
29. **Pham, L. M.** Magnetic Field Sensing with Nitrogen-Vacancy Color Centers in Diamond. *Doctoral dissertation, Harvard University.* 2013.
30. **Karaveli, S., et al.** Modulation of nitrogen vacancy charge state and fluorescence in nanodiamonds using electrochemical potential. *PNAS.* 2016, Vols. 113(15): 3938–3943.
31. **Carbonera, D.** Optically Detected Magnetic Resonance (ODMR) of photoexcited triplet states. *Photosynth Res. .* 2009, Vols. 102(2-3):403-14.
32. **Larsson, J. A. and Delaney, P.** Electronic structure of the nitrogen-vacancy center in diamond from first-principles theory. *Physical review.* 2008, Vol. 77.
33. **Delaneya, P. and Larsson, J.A.** Small cluster model of the NV centre in diamond. *Physics procedia .* 2010, Vols. 1533-1537.
34. **Maze, J. R., et al.** Properties of nitrogen-vacancy centers in diamond: the group theoretic approach. *New Journal of Physics.* 2011, Vol. 13.
35. **Rondin, L., et al.** Magnetometry with nitrogen-vacancy defects in diamond . *Edoc.* 2014.
36. **Nolte, S. and Oliver, E.** Development of a diamond-based scanning probe spin sensor operating at low temperature in ultra high vacuum. *OPUS.* 2014.
37. **Acosta, V. M., et al.** Optical properties of the nitrogen-vacancy singlet levels in diamond. *Physical review B.* 2010, Vol. 82: 201202.
38. **Appel, P., et al.** Nanoscale microwave imaging with a single electron spin in diamond. *New Journal of Physics .* 2015, Vol. 17.
39. **Hong, S., et al.** Nanoscale magnetometry with NV centers in diamond. *Mrs Bulletin.* 2013, Vol. 38.
40. **Faklaris, O., et al.** Photoluminescent nanodiamonds: Comparison of the photoluminescence saturation properties of the NV color center and a cyanine dye at the single emitter level, and study of the color center concentration under different preparation conditions. *Diamond & related materials.* 2010, Vols. 19: 988–995.
41. **Gulka, M.** Bio-Molecular sensors for molecular diagnostics in nanomedicine based on color centers in diamond. *Docteral Thesis.* 2017.
42. **Edwards, R. S., et al.** High field high frequency EPR techniques and their application to single molecule magnets. *Physica B: Condensed Matter.* 2014, Vols. 346–347.
43. **Balasubramanian, G., et al.** Nanoscale imaging magnetometry with diamond spins under ambient conditions. *Nature.* 2008, Vol. 455.
44. **Aiello, C. D., Hirose, M. and Cappellaro, P.** Composite-pulse magnetometry with a solid-state quantum sensor. *Nature communications.* 2013, Vol. 4.
45. **Pham, L. M., et al.** Magnetic field imaging with nitrogen-vacancy ensembles. *New Journal of Physics.* 2011, Vol. 13.

46. **Balaban, S. R. and Peters, D. C.** Basic principles of cardiovascular magnetic resonance. *Cardiovasculur magnetic resonance.* 2010, Vol. 2nd edition.
47. **Maclaurin, D., et al.** Nanoscale magnetometry through quantum control of nitrogen–vacancy centres in rotationally diffusing nanodiamonds. *New Journal of Physics.* 2013, Vol. 15.
48. **Hui, Y. Y., Cheng, C.-L. and Chang, H.-C.** Nanodiamonds for optical bioimaging. *Journal of physics D: Applied physics.* 2010.
49. **Cui, H., Kong, Y. and Zhang, H.** Oxidative Stress, Mitochondrial Dysfunction, and Aging. *Journal of signal transduction.* 2012.
50. **Yakovlev, R.Yu., et al.** Determination of impurities in detonation nanodiamonds by gamma activation analysis method. *Diamond & Related Materials.* 2015, Vols. 55: 77-86.
51. **Harrison, J., Sellars, M. J. and Manson, N. B.** Measurement of the optically induced spin polarisation of N-V centres in diamond. *Diamond and Related Materials.* 2005, Vols. 15, 4-8.
52. **Pham, L. M., et al.** Magnetic field imaging with nitrogen-vacancy ensembles. *New journal of medicine.* 2011, Vols. 13 - 045021.
53. **Aslam, N., et al.** Photo-induced ionization dynamics of the nitrogen vacancy defect in diamond investigated by single-shot charge state detection. *New journal of physics.* 2013.
54. **Gulka, M., et al.** Pulsed Photoelectric Coherent Manipulation and Detection of N-V Center Spins in Diamond. *Physical review applied.* 2017, Vol. 7: 044032 .
55. **Ermakova, A.** Single spins in diamond for nanoscale sensing and microscopy. *Doctoral thesis.* 2016.
56. **Uchi, J. O., Jhun, B. S. and Sheu, S. S.** Structural and molecular bases of mitochindrial ion channel function. *Advances in microbial physiology.* 2014, Vol. 6th edition.
57. **Sangtawesin, S., et al.** Hyperfine-enhanced gyromagnetic ratio of a nuclear spin in diamond. *New Journal of Physics.* 2016, Vol. 18.
58. **Wei, Y., et al.** Quantitative measurement of reactive oxygen species in vivo by utilizing a novel method: chemiluminescence with an internal fluorescence as reference. *Journal of Biomedical Optics.* 2010, Vol. 15.
59. **Tetienne, J.-P., et al.** Spin relaxometry of single nitrogen-vacancy defects in diamond nanocrystals for magnetic noise sensing. *Phys. Rev.* 2013, Vol. B 87.

Supplementary information

ODMR spectra of dried ND sample on a coverslip

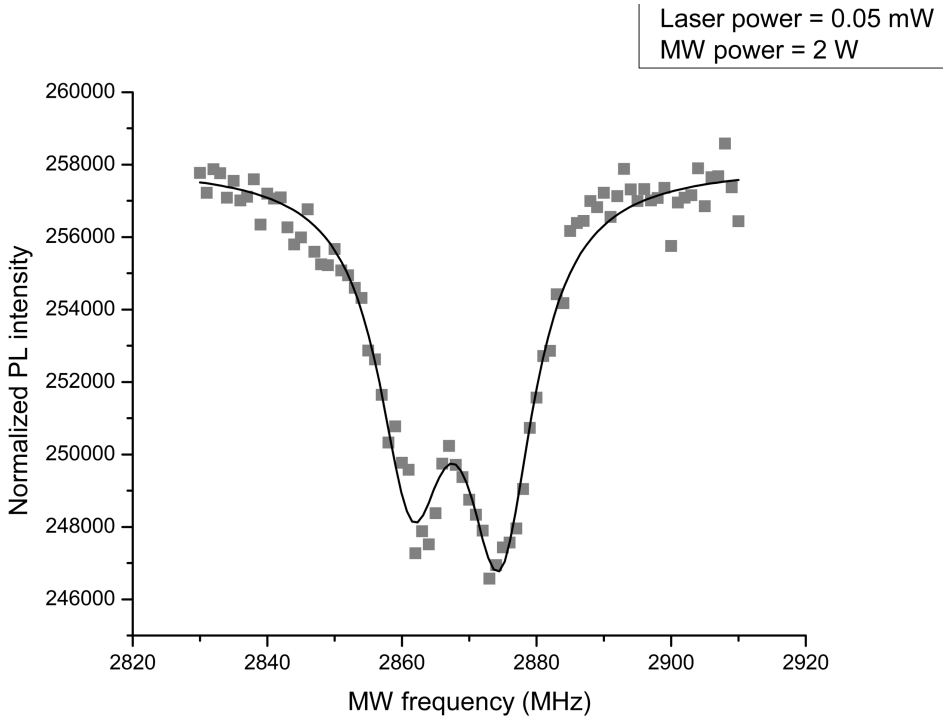

ODMR spectrum taken from a dried ND sample on a coverslip. Laser power of 0.05 mW and MW power of 2 W were used.

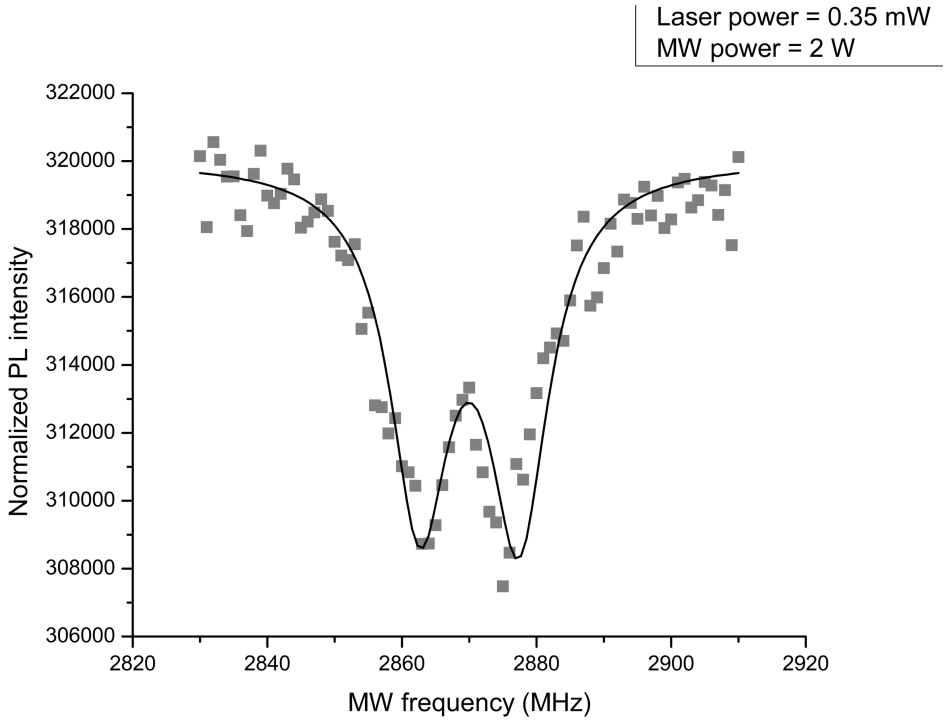

ODMR spectrum taken from a dried ND sample on a coverslip. Laser power of 0.35 mW and MW power of 2 W were used.

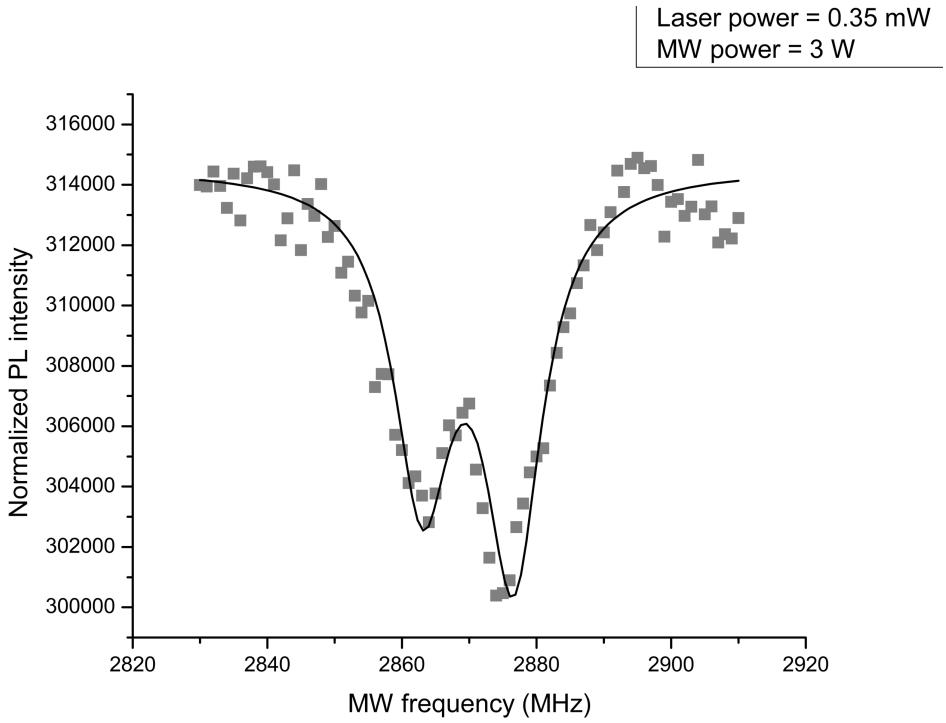

ODMR spectrum taken from a dried ND sample on a coverslip. Laser power of 0.35 mW and MW power of 3 W were used.

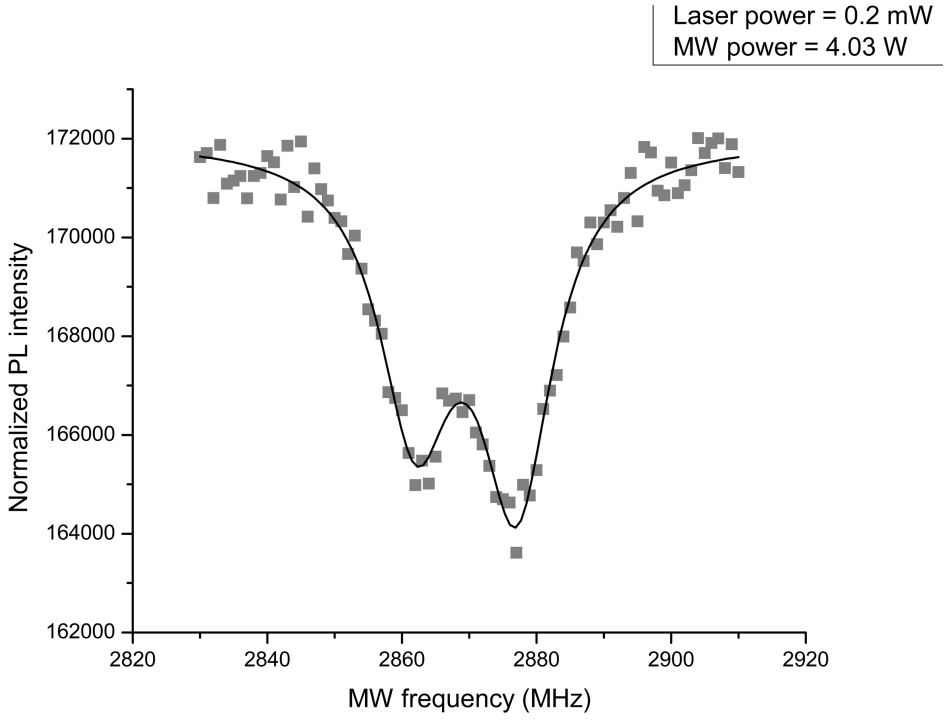

ODMR spectrum taken from a dried ND sample on a coverslip. Laser power of 0.2 mW and MW power of 4.03 W were used.

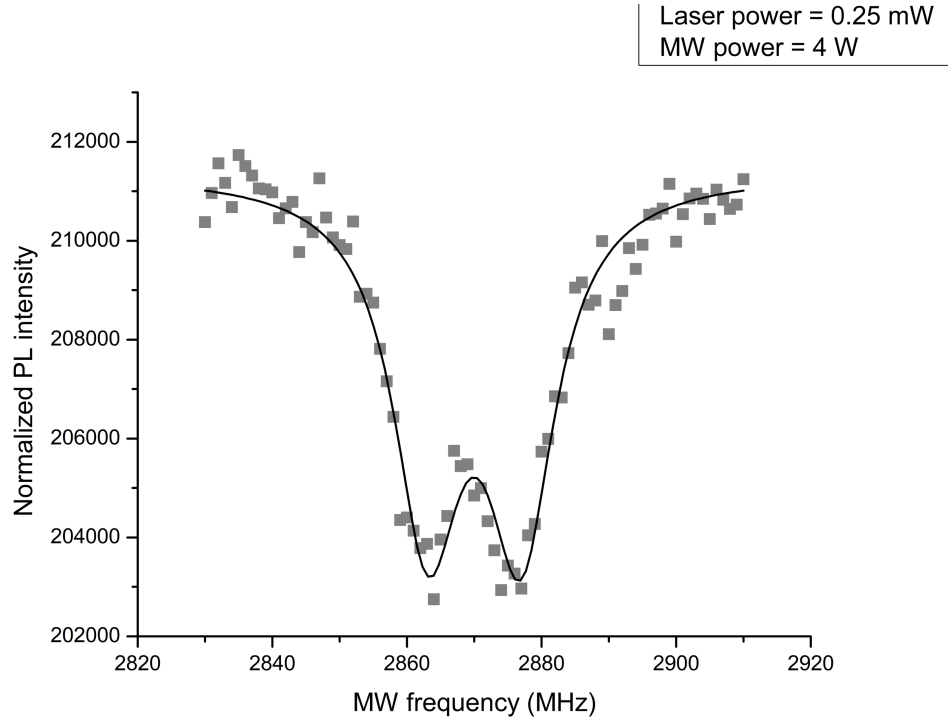

ODMR spectrum taken from a dried ND sample on a coverslip. Laser power of 0.25 mW and MW power of 4 W were used.

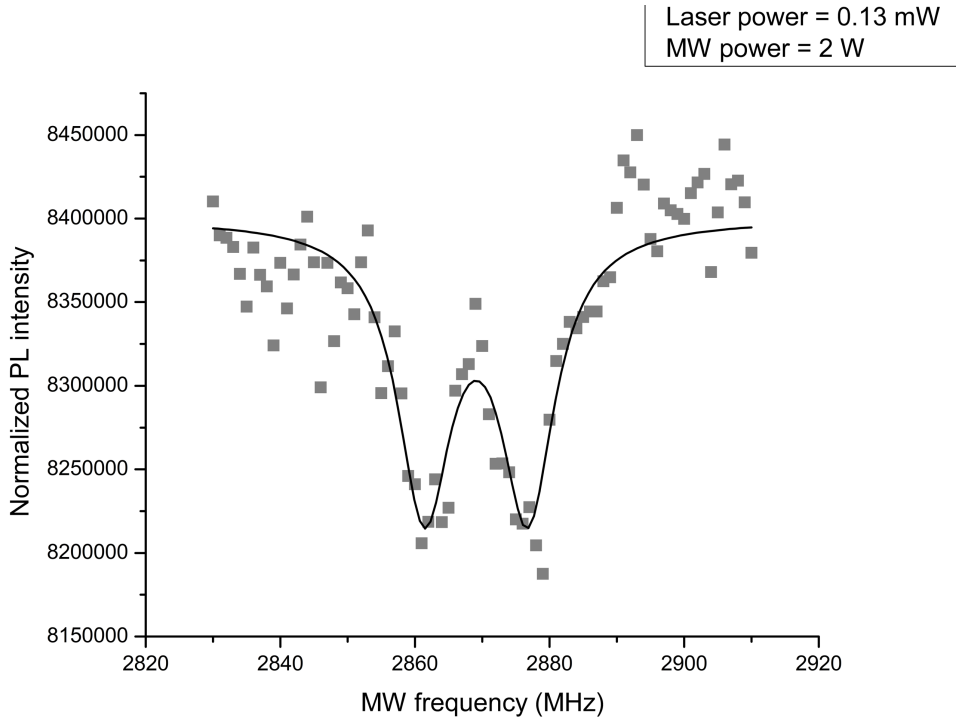

ODMR spectrum taken from a dried ND sample on a coverslip. Laser power of 0.13 mW and MW power of 2 W were used.

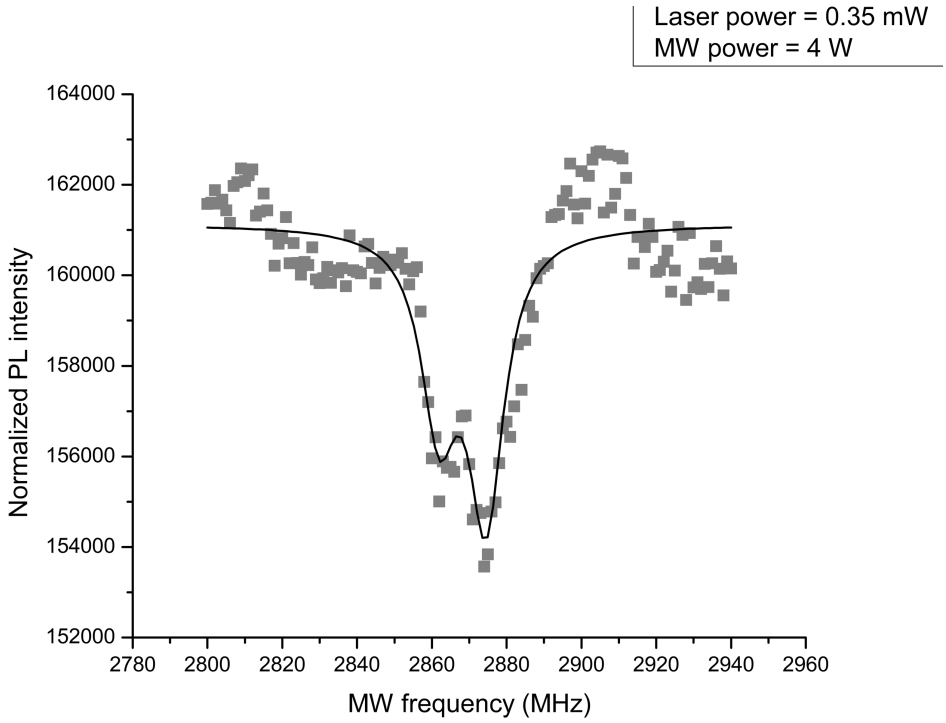

ODMR spectrum taken from a dried ND sample on a coverslip. Laser power of 0.35 mW and MW power of 4 W were used.

ODMR spectra in liquid

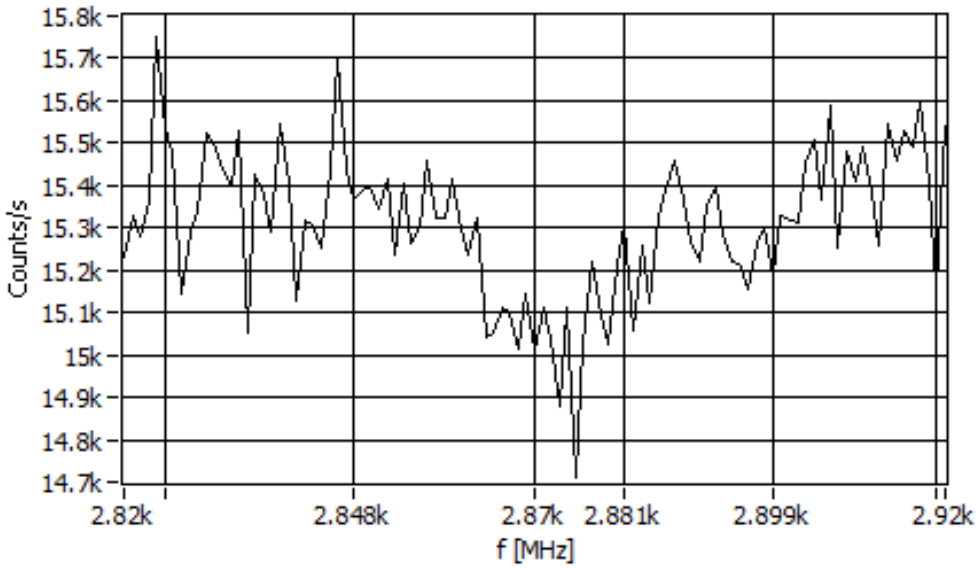

ODMR spectrum taken in liquid. ND concentration of 600 µg/ml together with a Laser power of 1.30 mW and MW power of 5 W were used.

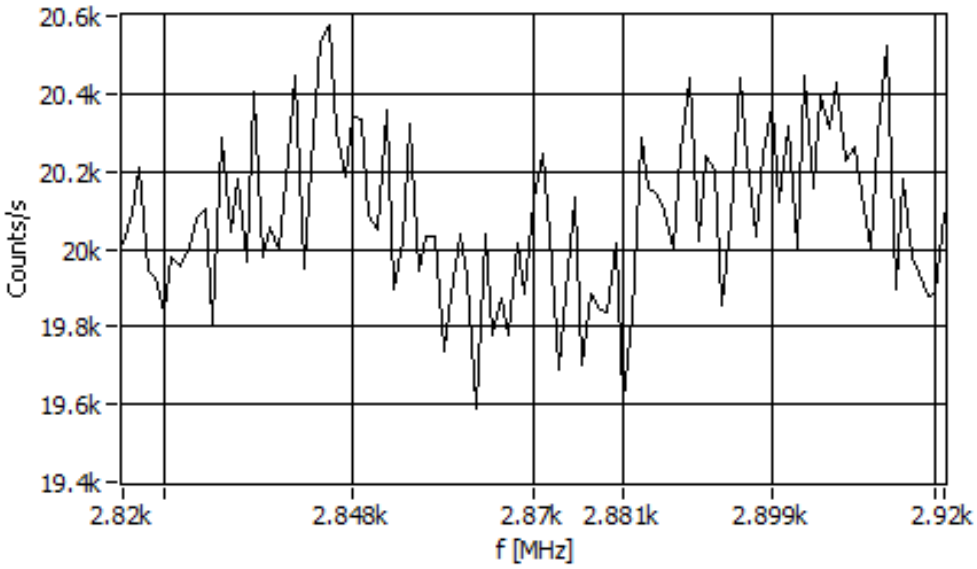

ODMR spectrum taken in liquid. ND concentration of 600 µg/ml together with a Laser power of 1.50 mW and MW power of 6 W were used.

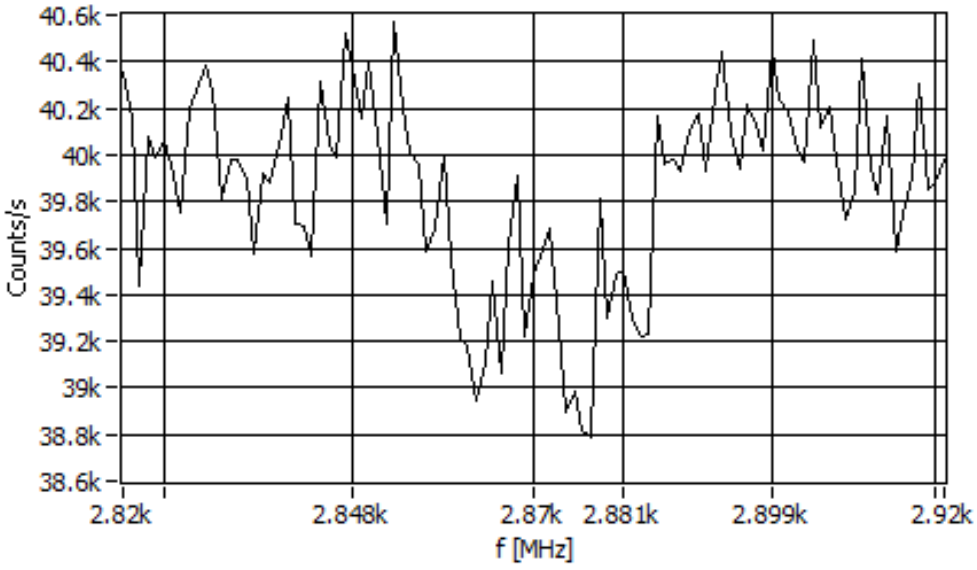

ODMR spectrum taken in liquid. ND concentration of 600 µg/ml together with a Laser power of 0.2 mW and MW power of 3 W were used.

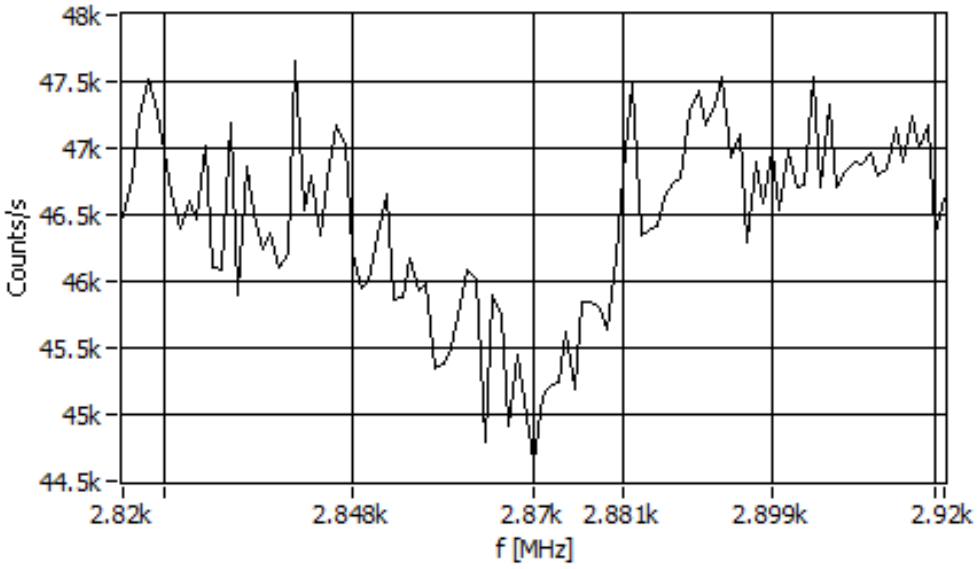

ODMR spectrum taken in liquid. ND concentration of 600 µg/ml together with a Laser power of 0.25 mW and MW power of 5 W were used.

Rabi measurements on single crystal diamond sample

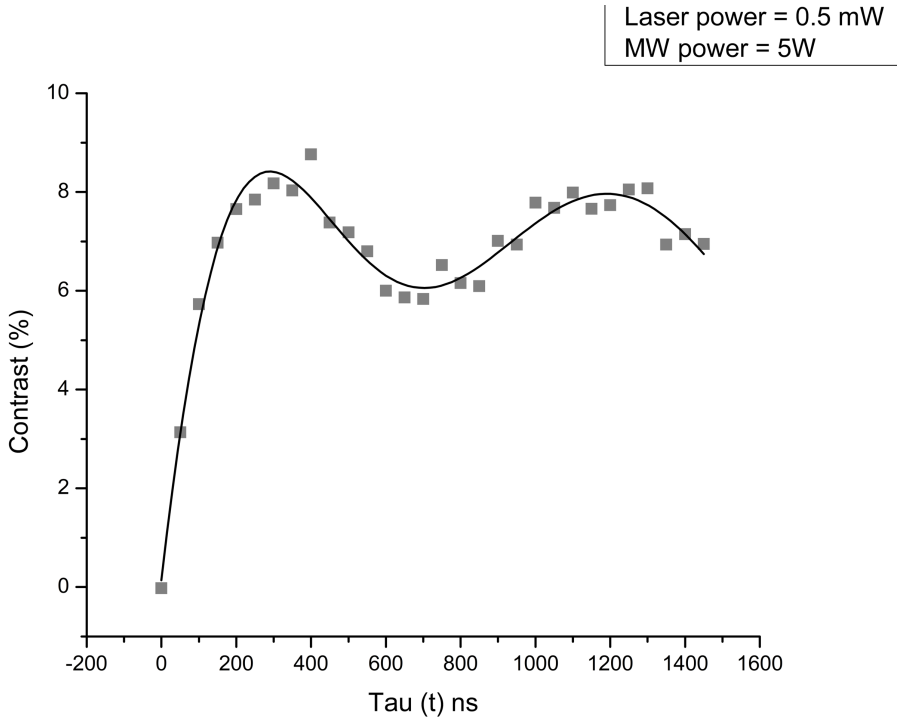

Rabi-oscillation measurements taken from a single crystal diamond sample. A laser power of 0.5 mW and a MW power of 5 W were used.

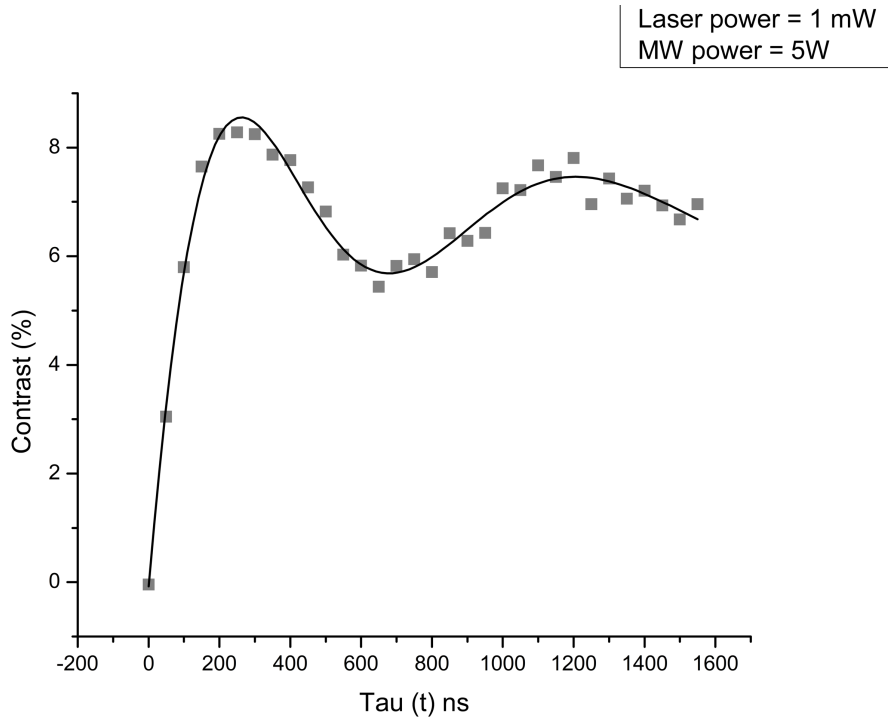

Rabi-oscillation measurements taken from a single crystal diamond sample. A laser power of 1 mW and a MW power of 5 W were used.

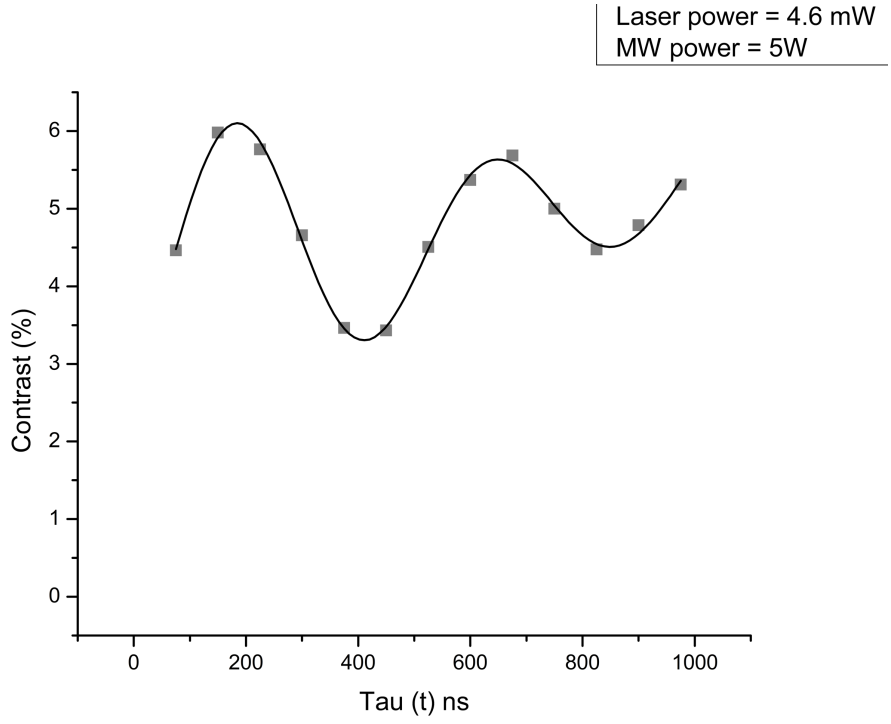

Rabi-oscillation measurements taken from a single crystal diamond sample. A laser power of 4.6 mW and a MW power of 5 W were used.

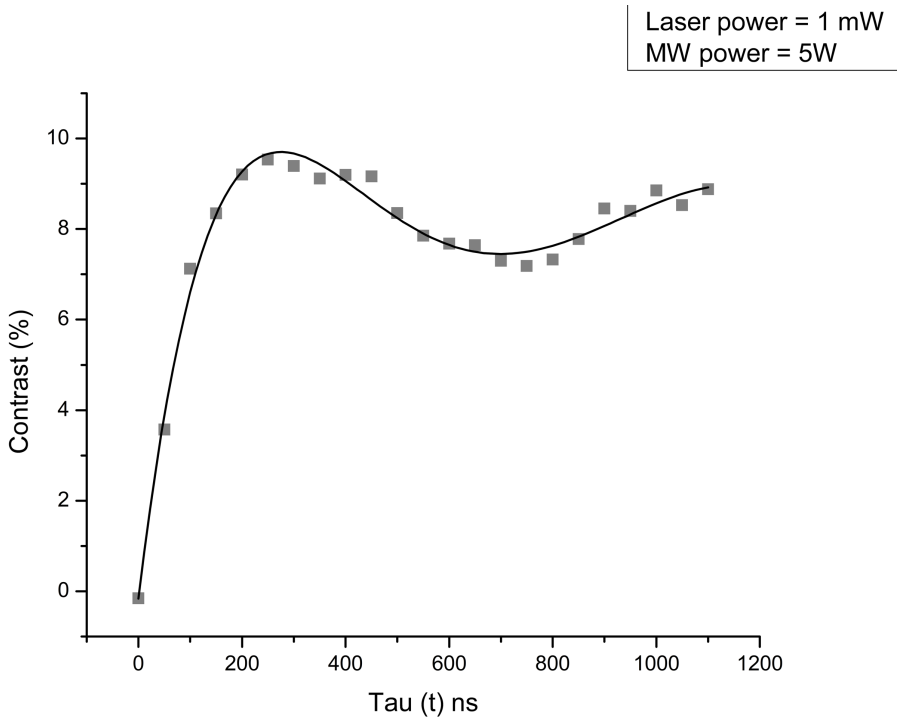

Rabi-oscillation measurements taken from a single crystal diamond sample. A laser power of 1 mW and a MW power of 5 W were used.

Rabi measurements on dried ND sample on a coverslip

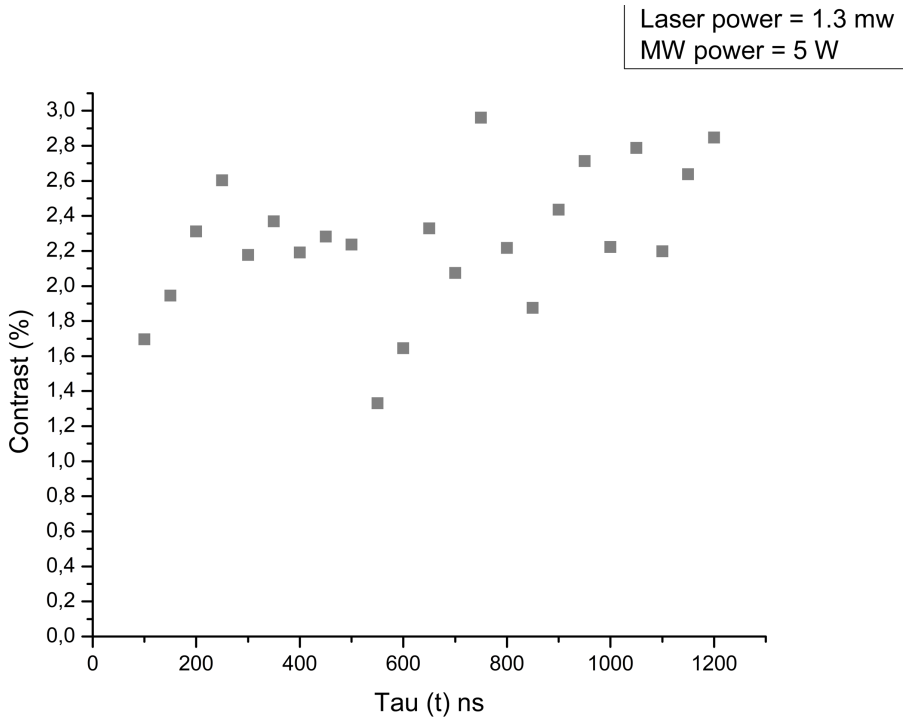

Rabi-oscillation measurements taken from a dried ND sample on a coverslip. A laser power of 1.3 mW and a MW power of 5 W were used. Fitting the results was impossible because the fitting program couldn't recognize a proper oscillating behavior.

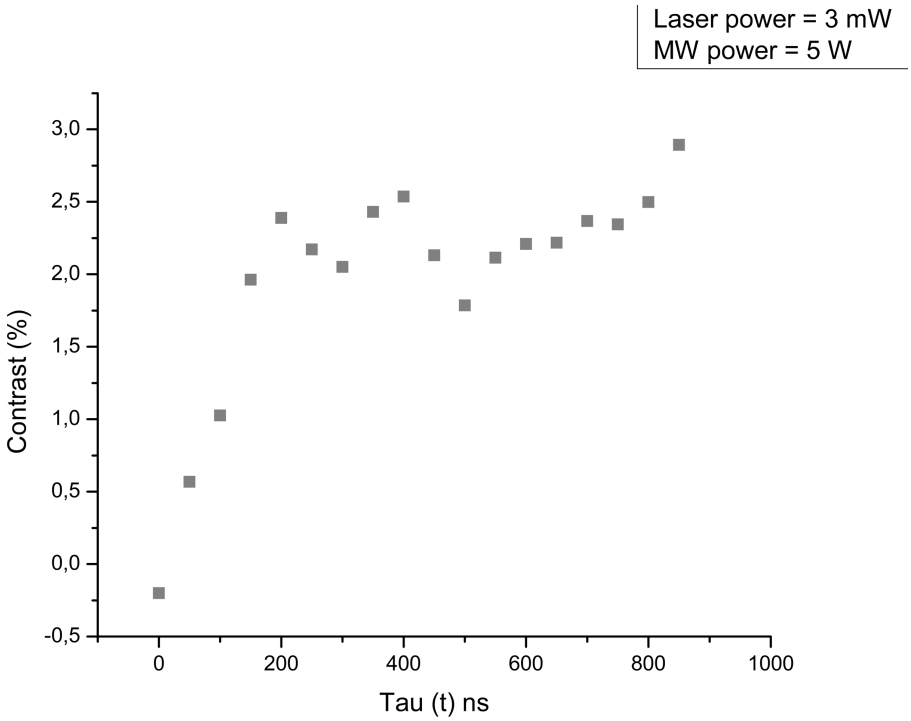

Rabi-oscillation measurements taken from a dried ND sample on a coverslip. A laser power of 3 mW and a MW power of 5 W were used. Fitting the results was impossible because the fitting program couldn't recognize a proper oscillating behavior.

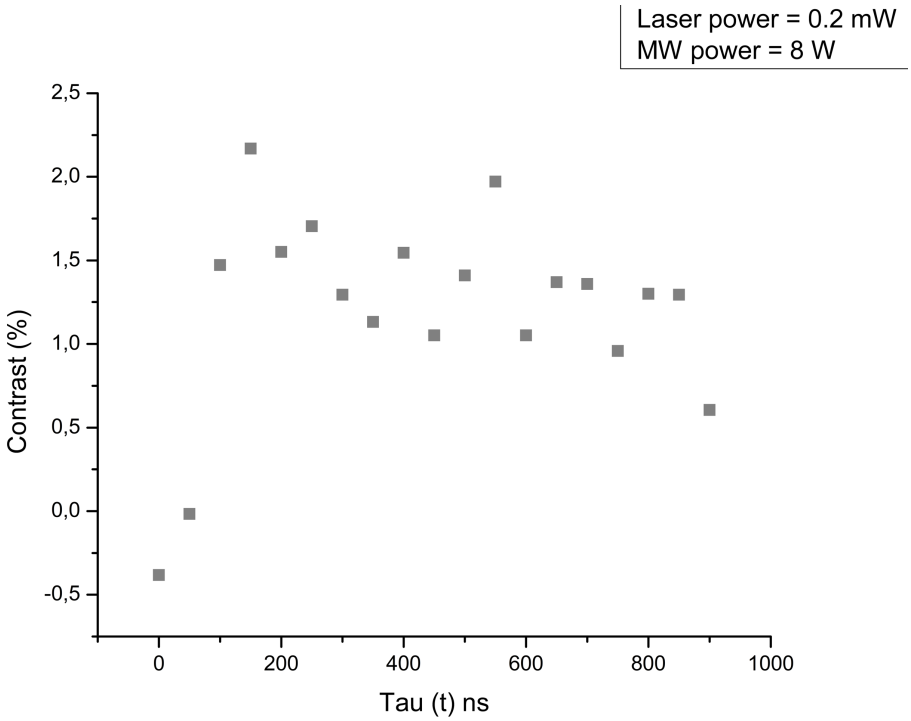

Rabi-oscillation measurements taken from a dried ND sample on a coverslip. A laser power of 0.2 mW and a MW power of 8 W were used. Fitting the results was impossible because the fitting program couldn't recognize a proper oscillating behavior.

T1 measurements on single crystal diamond sample

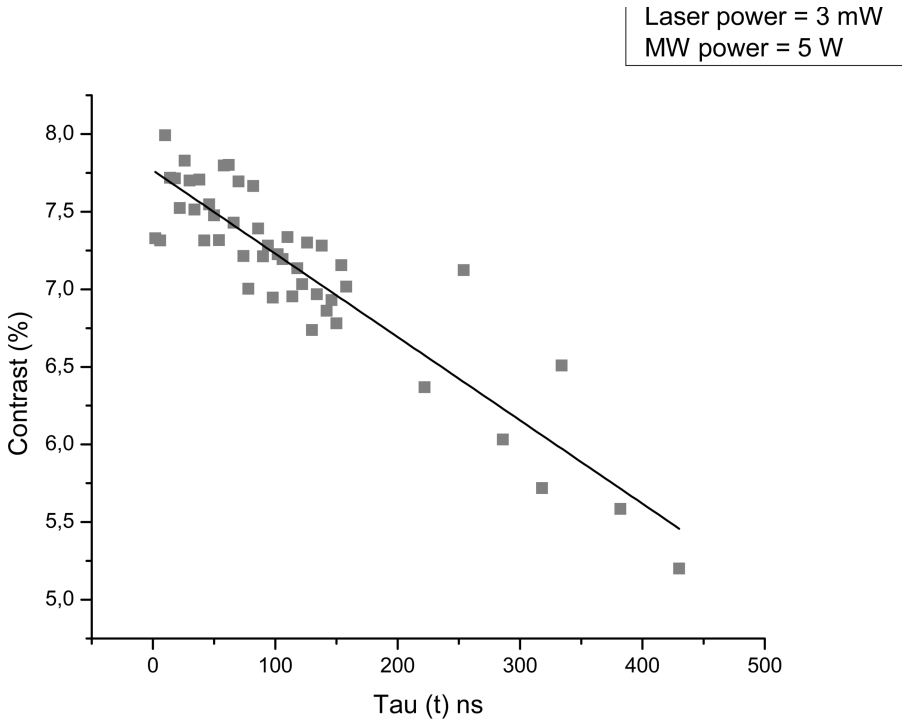

T1 relaxation time on single crystal diamond. Laser power was set at 3 mW, laser pulse duration at 1000 ns. For the MW power, 5W was used. The delay of the MW pulse was set at 300 ns. The π-pulse was 185 ns. The resulting T1 time was 3403 ns obtained from the fit.

Auteursrechtelijke overeenkomst

Ik/wij verlenen het wereldwijde auteursrecht voor de ingediende eindverhandeling:
Luminescent nanodiamonds: solution for precise molecular detection

Richting: **Master of Biomedical Sciences-Bioelectronics and Nanotechnology**
Jaar: **2018**

in alle mogelijke mediaformaten, - bestaande en in de toekomst te ontwikkelen - , aan de Universiteit Hasselt.

Niet tegenstaand deze toekenning van het auteursrecht aan de Universiteit Hasselt behoud ik als auteur het recht om de eindverhandeling, - in zijn geheel of gedeeltelijk -, vrij te reproduceren, (her)publiceren of distribueren zonder de toelating te moeten verkrijgen van de Universiteit Hasselt.

Ik bevestig dat de eindverhandeling mijn origineel werk is, en dat ik het recht heb om de rechten te verlenen die in deze overeenkomst worden beschreven. Ik verklaar tevens dat de eindverhandeling, naar mijn weten, het auteursrecht van anderen niet overtreedt.

Ik verklaar tevens dat ik voor het materiaal in de eindverhandeling dat beschermd wordt door het auteursrecht, de nodige toelatingen heb verkregen zodat ik deze ook aan de Universiteit Hasselt kan overdragen en dat dit duidelijk in de tekst en inhoud van de eindverhandeling werd genotificeerd.

Universiteit Hasselt zal mij als auteur(s) van de eindverhandeling identificeren en zal geen wijzigingen aanbrengen aan de eindverhandeling, uitgezonderd deze toegelaten door deze overeenkomst.

Voor akkoord,

Kruyfhooft, Louis

Datum: **7/06/2018**